

1 *We thank the Reviewer for the comments and suggestions to improve our paper. We feel the changes and*  
2 *additions we have made have improved the paper and provide a much better manuscript for the HESS*  
3 *audience. We have addressed each comment individually, below:*

4 **ANONYMOUS REFEREE #2**

5 **RECEIVED AND PUBLISHED: 4 AUGUST 2014**

6 **The paper addresses the important topic of providing urban land models with accurate inputs related**  
7 **to the surface properties. The authors derive a set of properties from satellite data (most notably leaf**  
8 **area index, green vegetation fraction, and impervious surface area) and provide them as inputs to the**  
9 **offline NOAA-UCM urban model to compare the resulting outputs to those obtained with the default**  
10 **tabulated model input. They proceed to perform a sensitivity analysis of the model and then to assess**  
11 **the influence of the new parameters on the model's ability to match observations.**

12 **The paper is in general interesting and well written but some major revisions are needed.**

13 **MAJOR COMMENTS:**

14 **The authors write in the conclusions: "Nevertheless, the model still underestimates remotely sensed**  
15 **LST values, over highly developed areas. We speculate that the underestimation of LST values,**  
16 **particularly over high intensity residential and industrial/ commercial areas, is due to structural**  
17 **parameterization in the UCM and cannot be immediately solved with available parameter choices." In**  
18 **other parts they attribute this to a phase-lag in the discretization of the UCM. While this phase lag**  
19 **might play a role, an inconsistency that was recently pointed out in NOAA-UCM is that over urban**  
20 **terrain the model in fact computes the surface temperature of a homogeneous grass field that**  
21 **exchanges the same sensible heat flux with the atmosphere as the urban mix in the pixel. This is not**  
22 **the true urban temperature one (or satellites) would sense. WRF-UCM computes the fluxes from each**  
23 **subfacet (urban grass, roofs, urban canyons) separately and correctly but then uses the thermal**  
24 **roughness length of grass to infer a surface temperature. It is possible to compute a physically**  
25 **relevant surface temperature from WRF-UCM from the outputs it provides. I strongly encourage the**  
26 **authors to check the following reference for the details and potentially compute the surface**  
27 **temperature as done in that reference: Li, D., & Bou-Zeid, E. (2014). Quality and sensitivity of high-**  
28 **resolution numerical simulation of urban heat islands. Environmental Research Letters, 9(5), 055001.**  
29 **doi:10.1088/1748-9326/9/5/055001.**

30 **We thank the reviewer for this helpful comment. We re-ran the simulations, adopting the revised**  
31 **calculation of LST proposed by Li and Bou-Zeid [2014]. Using the new approach, the LST values over**  
32 **highly developed surfaces are significantly increased. This solves the LST underestimation problem in**  
33 **these areas (see revised Figs. 5 and 6). To implement the revised LST calculation, the following changes**  
34 **were made to the manuscript:**

35 **The following section is **ADDED** to the manuscript:**

36 ***"4.3. Improving the UCM-simulated LST***

37 The calculation of the impervious surface temperature in the UCM version used in this study has been  
38 shown to be inaccurate [Li and Bou-Zeid, 2014]. This is due to the fact that the turbulent transfer  
39 coefficient ( $C_h$ ) for the whole pixel is calculated using only momentum and thermal roughness lengths of  
40 vegetated portion, ignoring the developed surface impact on  $C_h$ . Li and Bou-Zeid [2014] showed that this  
41 inconsistency could result in large biases in simulated LST values. In the current study, an alternative LST  
42 calculation, proposed by Li and Bou-Zeid [2014], is used as follows. First, a revised surface temperature of  
43 the impervious part of the pixel ( $T_s$ ) is calculated based on canyon temperature ( $T_c$ ) and roof surface  
44 temperature ( $T_r$ ):

$$45 \quad T_s = f_r \times T_r + (1 - f_r) \times T_c \quad \text{Eq. (12)}$$

46 where  $f_r$  is the roof fraction of the impervious surface. Note that the  $T_c$  calculated by the UCM is an  
47 equivalent aerodynamic surface temperature aggregated for canyon surfaces, including walls and roads.  
48 Next, the LST for the whole grid cell is computed as a weighted average based on the  $T_s$  and surface  
49 temperature of pervious part ( $T_1$ ):

$$50 \quad LST = f_{urb} \times T_s + (1 - f_{urb}) \times T_1 \quad \text{Eq. (13)}$$

51 where  $f_{urb}$  is the urban fraction of the pixel."

52 The following is **REMOVED** from the manuscript (abstract):

53 "However, the model still underestimates remotely sensed LST values over highly developed areas. We  
54 hypothesize that the LST underestimation is due to structural formulation in the UCM and cannot be  
55 immediately solved with available parameter choices."

56 The followings are **REMOVED** from the manuscript (section 7.2):

57 "Further analysis (not shown here) indicates that underestimation of LST values is due to a fundamental  
58 problem in the UCM and cannot be immediately solved with available parameter choices. This problem is  
59 discussed in a related study investigating different schemes for LST and conductive heat fluxes in the  
60 UCM [Wang et al. 2011b]. Their study shows that the current UCM formulation results in a phase lag and  
61 cold biases in simulated surface temperature when compared to observations. The discussed cold biased  
62 could potentially be resolved utilizing a spatially-analytical scheme introduced by Wang et al. [2011b]."

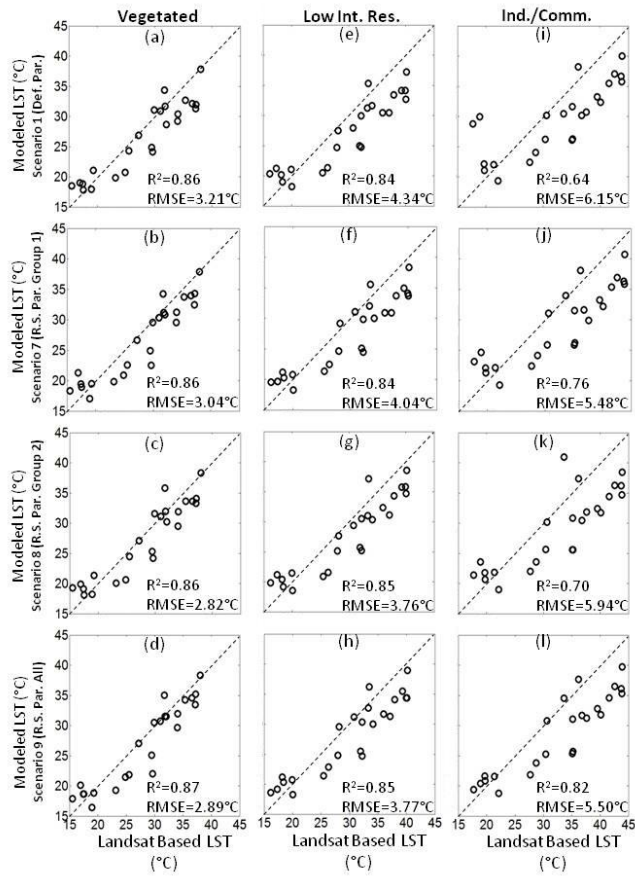
63 "Regardless of the parameterization processes, cold biases are persistent in all simulations, particularly  
64 over high intensity residential and industrial/commercial pixels (Fig. 6). As explained above, this  
65 underestimation of LST values is consistent with the literature and is reported to be due to a fundamental  
66 problem in the UCM which produces a phase lag and cold biases in simulated LST [Wang et al., 2011b]."

67 The following is **REMOVED** from the manuscript (section 8):

68 "Nevertheless, the model still underestimates remotely sensed LST values, over highly developed areas.  
69 We speculate that the underestimation of LST values, particularly over high intensity residential and

70 industrial/commercial areas, is due to structural parameterization in the UCM and cannot be  
71 immediately solved with available parameter choices."

72 The following figure is **REMOVED** from the manuscript:



73  
74 **Figure 5. Scatter plots of observed (Landsat-based) versus simulated LSTs averaged over different land cover**  
75 **types using different urban surface parameterizations, including scenarios 1 (first row), 7 (second row), 8 (third**  
76 **row), and 9 (forth row) in Table 1.**

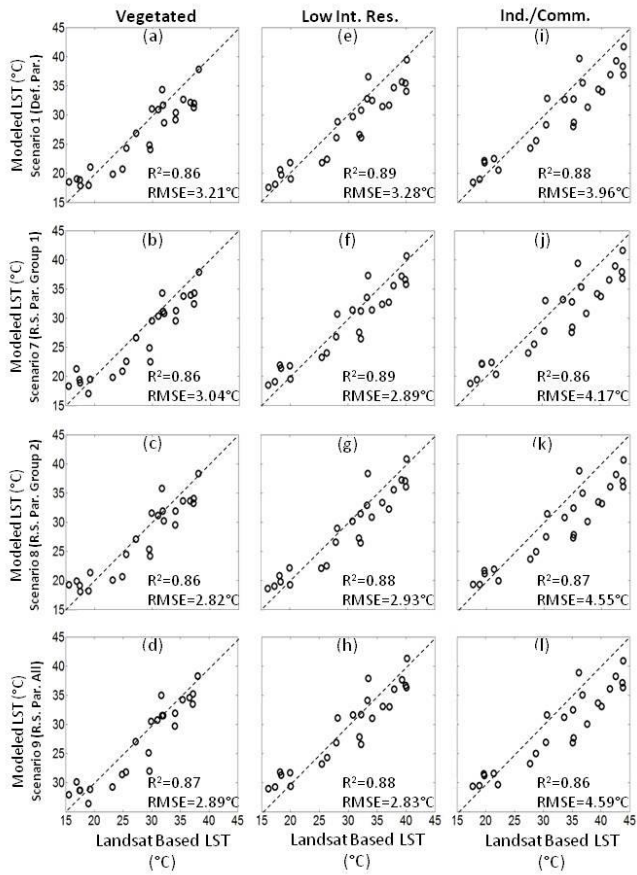
77  
78  
79

80

81

82

83 The following figure is **ADDED** to the manuscript:



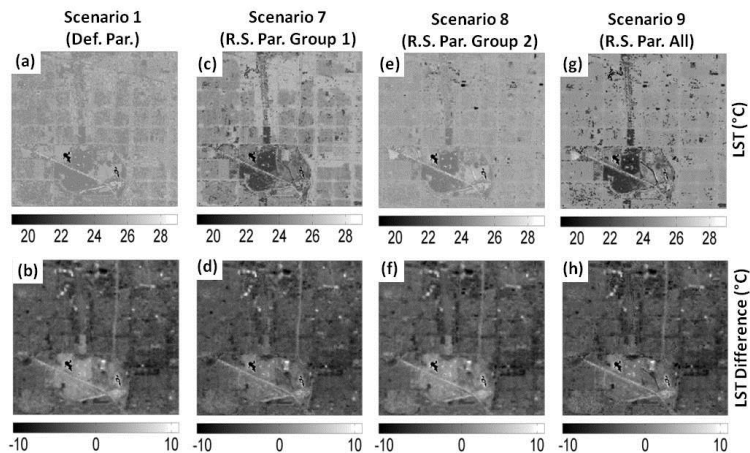
84

85 **Figure 5. Scatter plots of observed (Landsat-based) versus simulated LSTs averaged over different land cover**  
86 **types using different urban surface parameterizations, including scenarios 1 (first row), 7 (second row), 8 (third**  
87 **row), and 9 (fourth row) in Table 1.**

88

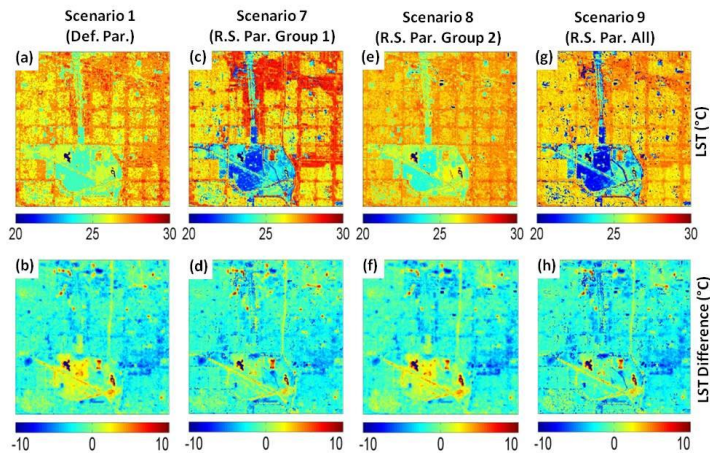
89

90 The following figure is **REMOVED** from the manuscript:



91  
92 **Figure 6. Noah/UCM simulated LST maps using different urban surface parameterizations: scenarios 1, 7, 8, and**  
93 **9 from Table 1 (top row) as well as differences between simulated and observed land surface temperature at**  
94 **1100 LST on 14 April 2011 (bottom row).**

95 The following figure is **ADDED** to the manuscript:



96  
97 **Figure 6. Noah/UCM simulated LST maps using different urban surface parameterizations: scenarios 1, 7, 8, and**  
98 **9 from Table 1 (top row) as well as differences between simulated and observed land surface temperature at**  
99 **1100 LST on 14 April 2011 (bottom row).**

100

101 References:

102 Li, D., E. Bou-Zeid, 2014: Quality and Sensitivity of High-Resolution Numerical Simulation of Urban Heat  
103 Islands. Environmental Research Letters, 9, 055001 doi:10.1088/1748-9326/9/5/055001

104 **When computing albedo or emissivity from satellite data, I presume the result is some sort of an**  
105 **effective/average albedo or emissivity over the whole pixel. But for urban grid cells or pixels in NOAH-**  
106 **UCM, these parameters are imposed separately for the vegetated fraction of the cell, the roof, the**  
107 **walls, and the impervious ground surfaces (almost like a tiling or MOSAIC approach). It is unclear how**  
108 **the authors imposed these values in NOAH-UCM . Did they impose the same values for all facets? Did**  
109 **they use these only for the vegetated fraction (which would be problematic), etc. The authors should**  
110 **clarify what parameters in NOAH-UCM they override over urban pixels.**

111 In the current study the remotely sensed albedo and emissivity value for each pixel are assigned to both  
112 pervious and impervious surfaces for that pixel.

113 We agree with the reviewer's comment and **added** the following to the section 5.1 to clarify the  
114 approach taken to implement the remotely sensed parameters:

115 *"However, remotely sensed albedo and emissivity values over each pixel are assigned to both pervious*  
116 *and impervious surfaces for that pixel."*

117 **The figures are extremely difficult to read. The different line types are very similar and I don't know**  
118 **why the authors do not use different colors since color figures are free in HESS anyway. If it is to allow**  
119 **B/W printing (which I think they should not worry about that much) then they should try to make the**  
120 **line types easier to distinguish.**

121 We agree with the reviewer's comment. Most of the figures are reproduced in color in the revised  
122 submission.

123 **Page 7477, lines 16-17. Are these values from Stenberg et al. (2004) derived for urban areas in that**  
124 **study? If not, do the authors expect different results over urban terrain?**

125 No, the LAI values in the current study are independent from the study done in Stenberg et al. (2004). In  
126 the current study, LAI values are retrieved based on the LAI-RSR correlations utilizing table-based LAI  
127 estimates in pure pixels and remote sensing based RSR maps.

128 Yes, we believe the LAI patterns calculated over Los Angeles metropolitan area illustrate a unique  
129 behavior particularly at temporal scale. The LAI values do not show a strong seasonal variation, as it is  
130 common in other areas.

131 **NOAH-UCM to the best of my knowledge requires atmospheric fields at some elevation above the**  
132 **buildings. On page 7481 the authors describe driving it with measurements at 2m. Is that accurate?**  
133 **Can it be run with inputs at that height or did they have to extrapolate to some higher elevation?**

134 We thank the reviewer for this comment. We used the measurements at 2m to force the Noah-UCM to  
135 avoid additional uncertainties involved in converting 2m observations to top of the roof values. We  
136 expect the resulting error to be minimal as the average building height is close to 2m for our study  
137 domain which does not include the downtown LA area with tall buildings.

138 **Page 7482, lines 5-8 are unclear. An equation might help. Are they referring to the point they describe**  
139 **before about increasing these values since the remote sensing data presumes they are spread over**  
140 **the whole pixel?**

141 We agree with the reviewer's comment and **added** the following the manuscript to clarify the  
142 mentioned approach:

143 *"It should be noted that the GVF and LAI measurements over mixed pixels (vegetated urban areas) are*  
144 *scaled up by multiplying the remotely sensed values by  $1/(1-\text{urban fraction})$  since in the Noah-UCM*  
145 *modeling framework these parameters characterize only the pervious portion ( $1 - \text{urban fraction}$ ) of each*  
146 *pixel."*

147 **Have the authors tried to look at the impact of shorter time steps since most tests of NOAA-UCM are**  
148 **in online mode where the time steps are much shorter? I think a test showing insensitivity to the time**  
149 **step would be useful since 1 hour is not much shorter than other significant times scales related to the**  
150 **surface such as the conductive time scale in the surface.**

151 We thank the reviewer for this comment.

152 No, we have not conducted simulations with shorter time steps for the current study. However, the  
153 authors have studied the insensitivity of Noah-UCM to the time scales shorter than one hour on  
154 separate projects but in the same area. The time step of 1 hr was chosen based on the temporal scale of  
155 observations used to force the model (1 hr), the degree to which we needed this temporal resolution to  
156 capture the diurnal variability in our domain, and the authors' prior experience in land surface modeling.

157 **Page 7488: I am a bit surprised that "The changes in absolute surface albedos do not affect simulated**  
158 **latent heat fluxes (Fig. 3I)." Any explanation for that? The albedo alters available energy and should**  
159 **influence both H and LE.**

160 We agree with the reviewer's comment about the impact of albedo changes on simulated turbulent  
161 fluxes. The lack of albedo induced changes on simulated latent heat flux may be due to the fact that the  
162 changes in the albedo values, after using remote sensing data, are minimal (see Fig. 3: note that the  
163 color bar scale is relatively small, ranging from 0 to 0.4) except for isolated buildings with bright roofs  
164 which are located in the industrial/commercial pixels with negligible pervious fraction and latent heat  
165 flux.

166 To address this comment we **added** the following to the manuscript (section 6.2):

167 *"The sensible heat flux differences are only significant over industrial/commercial pixels which include*  
168 *buildings with bright roofs (up to  $\sim 300 \text{ W m}^{-2}$ ; Fig. 3k). The changes in absolute surface albedos do not*

169 *affect simulated latent heat fluxes as these reflective roofs are located in industrial/commercial areas*  
170 *with negligible pervious surfaces and simulated latent heat flux (Fig. 3)."*

171 **MINOR COMMENTS**

172 **Page 7472 line 12: replace "Tahah" by "Taha".**

173 We appreciate the reviewer's comment. The change is made.

174 **Page 7473 line 3: replace "later" by "layer".**

175 We appreciate the reviewer's comment. The change is made.

176 **Page 7482, lines 8: replace "sending" by "sensing".**

177 We appreciate the reviewer's comment. The change is made.

178 **Page 7491, lines 21: replace "result" by ", resulting".**

179 We appreciate the reviewer's comment. The change is made.

180 **Results in figure 4: are these averaged over all individual CIMIS stations and corresponding pixels? Or**  
181 **did they use flux maps interpolated from CIMIS and then compare to the whole model domain? The**  
182 **averaging in the figure is unclear.**

183 We created the interpolated maps of ET using inverse-distance weighting (2<sup>nd</sup> power) approach and then  
184 compared averaged values over fully vegetated pixel.

185 To address the reviewer's comment the following (underlined) is **added** to the manuscript (section 5.2.:  
186 Model Evaluation Approach):

187 *"This coefficient and  $ET_0$  estimations from ten CIMIS stations within close proximity of the study domain*  
188 *(Fig. 1a) are utilized to compute the urban landscape ET. Inverse-distance weighting (2<sup>nd</sup> power) is*  
189 *employed to create spatial gridded ET maps over fully vegetated pixels in the study area which is then*  
190 *used in validation processes of the Noah-UCM."*

191 The following (underlined) is **added** to the manuscript (section 7.1):

192 *"The temporal variations of ET, simulated by the Noah-UCM model and averaged over fully vegetated*  
193 *pixels, are evaluated against CIMIS-based ET measurements, spanning 2010 and 2011 (Fig. 4). The*  
194 *presented observations are averages over fully vegetated pixels in the study domain, calculated using ET*  
195 *maps based on  $ET_0$  measurements from ten CIMIS stations, landscape coefficients, and inverse-distance*  
196 *weighting (2<sup>nd</sup> power) (see section 5.2)."*

197 The following (underlined) is **added** to the Fig. 4 caption:

198 *"Figure 4. Noah/UCM simulated cumulative monthly ET, averaged over fully vegetated pixels using*  
199 *different urban surface parameterizations..."*



200 **Caption of figure 2: mention that fully vegetated corresponds to row 2, etc.**

201 We appreciate the reviewer's comment. The change is made.

202 **The symbols in figure 7 are not defined anywhere.**

203 We agree with the reviewer's comment. The following is **added** to the Figure 7 caption to address this  
204 issue:

205 *"Energy budget terms include: shortwave radiation (SW), longwave radiation (LW), and sensible (SH),*  
206 *latent (LH), and ground (GH) heat fluxes. Water budget terms include: precipitation (PPT), irrigation*  
207 *water (IRR), evapotranspiration (ET), surface runoff (SFC R.O.), and sub-surface runoff (S.SFC R.O.)."*

208

209

210

211

212

213

214

215

216

217

218

219

220

221

222

223

224

225 **High Resolution Land Surface Modeling Utilizing Remote Sensing Parameters and the Noah-**  
226 **UCM: A Case Study in the Los Angeles Basin**

227

228 **P. Vahmani<sup>1</sup> and T.S. Hogue<sup>2,1</sup>**

229 <sup>1</sup>University of California, Los Angeles, CA

230 <sup>2</sup>Colorado School of Mines, Golden, CO

231

232 Re-submission to HESS

**Deleted:** Submitted

233 October 2014

**Deleted:** April

234

235 *Corresponding Author:*  
236 Terri S. Hogue  
237 Civil and Environmental Engineering  
238 Colorado School of Mines  
239 1500 Illinois Street  
240 Golden, CO 80401  
241 [thogue@mines.edu](mailto:thogue@mines.edu)  
242 303-384-2588  
243

246 **ABSTRACT**

247 In the current work we investigate the utility of remote sensing based surface parameters in the Noah-  
248 UCM (urban canopy model) over a highly developed urban area. Landsat and fused Landsat-MODIS data  
249 are utilized to generate high resolution (30 m) monthly spatial maps of green vegetation fraction (GVF),  
250 impervious surface area (ISA), albedo, leaf area index (LAI), and emissivity in the Los Angeles  
251 metropolitan area. The gridded remotely sensed parameter datasets are directly substituted for the  
252 land-use/lookup-table-based values in the Noah-UCM modeling framework. Model performance in  
253 reproducing ET (evapotranspiration) and LST (land surface temperature) fields is evaluated utilizing  
254 Landsat-based LST and ET estimates from CIMIS (California Irrigation Management Information System)  
255 stations as well as in-situ measurements. Our assessment shows that the large deviations between the  
256 spatial distributions and seasonal fluctuations of the default and measured parameter sets lead to  
257 significant errors in the model predictions of monthly ET fields (RMSE= 22.06 mm/month). Results  
258 indicate that implemented satellite derived parameter maps, particularly GVF, enhance the Noah-UCM  
259 capability to reproduce observed ET patterns over vegetated areas in the urban domains (RMSE= 11.77  
260 mm/month). GVF plays the most significant role in reproducing the observed ET fields, likely due to the  
261 interaction with other parameters in the model. Our analysis also shows that remotely sensed GVF and  
262 ISA improve the model capability to predict the LST differences between fully vegetated pixels and  
263 highly developed areas.

264 **Key words: Noah LSM, UCM, remote sensing, urban hydrology, evapotranspiration, Los Angeles**

**Deleted:** However, the model still underestimates remotely sensed LST values over highly developed areas. We hypothesize that the LST underestimation is due to structural formulation in the UCM and cannot be immediately solved with available parameter choices.

270 **1. Introduction**

271 Urbanization introduces significant changes to land surface characteristics that ultimately perturb land-  
272 atmosphere fluxes of sensible heat, latent heat, and momentum which, in turn, alter atmospheric  
273 properties as well as local weather and climate [Landsberg, 1981; Kalnay and Cai, 2003; Miao et al.,  
274 2009; Ridder et al., 2012]. Urban surfaces are covered with variety of materials with distinct thermal,  
275 radiative, and moisture properties influencing surface energy and water budgets [Arnfield, 2003].  
276 Moreover, contrasting aerodynamic properties of buildings significantly change surface roughness  
277 [Cotton & Pielke, 1995]. The effects associated with modified urban landscapes extend to air quality  
278 [Taha et al., 1997], local temperatures [Bornstein, 1987; Van Wevenberg et al., 2008], local and regional  
279 atmospheric circulation [Pielke et al., 2002; Marshall et al., 2004; Niyogi et al., 2006], and regional  
280 precipitation patterns [Changnon and Huff, 1986; Changnon, 1992; Lowry, 1998].

281 Mesoscale meteorological models have been increasingly applied over urban areas to examine  
282 the urban-atmosphere exchange of heat, moisture, momentum or pollutants. Recently updated  
283 parameterization in the community Weather Research and Forecasting (WRF) model includes coupling  
284 between the Noah LSM (Land Surface Model) and a single layer urban canopy model (UCM) [Kusaka et  
285 al. 2001; Kusaka and Kimura, 2004] which has substantially advanced the understanding and modeling  
286 of the mesoscale impact of cities. The coupled WRF-Noah-UCM has been applied to major metropolitan  
287 regions around the world (e.g. Houston, Beijing, Guangzhou/Hong Kong, , Salt Lake City, and Athens) to  
288 better understand the contribution of urbanization to changes in urban heat island, surface ozone,  
289 horizontal convective rolls, boundary layer structure, contaminant transport and dispersion, and heat  
290 wave events [Chen et al., 2004; Jiang et al., 2008; Miao and Chen, 2008; Miao et al., 2009; Wang et al.,  
291 2009; Tewari et al., 2010; Wei-guang et al., 2011; Giannaros et al., 2013]. A common concern with the  
292 use of these complex mesoscale models, however, is the high level of uncertainty in the specification of  
293 surface cover and geometric parameters [Loridan et al., 2010; Chen et al., 2011]. Although realistic

294 representation of surface properties is critical for accurate simulation of the physical processes  
295 occurring in urban regions, the majority of previous modeling studies rely on traditional land-use data  
296 and lookup tables to define surface parameters.

297 Remote sensed observations provide important spatial information on urban-induced physical  
298 modifications to the Earth's surface [Jin and Shepherd, 2005]. Airborne LIDAR (Light Detection and  
299 Ranging) systems and photogrammetric techniques have been utilized to produce morphological  
300 parameters over urban areas [Burian et al., 2004, 2006, 2007; Taha, 2008; Ching et al., 2009]. Burian et  
301 al. [2004] used airborne LIDAR data, at 1 m resolution, to generate datasets of 20 urban canopy  
302 parameters (e.g., building height, height-to-width ratio, and roughness length) for an air quality  
303 modeling study over Houston, Texas. ~~Taha~~ [2008] introduced an alternative and low-cost approach for  
304 generating urban canopy parameters input for the uMM5 over Sacramento region, California. The study  
305 relied on commercially available Google Earth PRO imagery to generate urban geometry parameters  
306 (e.g., pavement land-cover fraction, roof cover fraction, and mean building height). Using LIDAR-based  
307 three-dimensional data sets of buildings and vegetation, Ching et al. [2009] presented a high-resolution  
308 database of the geometry, density, material, and roughness properties of the morphological features for  
309 applications in WRF and other models over Houston, Texas. While promising, the availability of such  
310 datasets is currently limited to a few geographical locations and the reproduction of such datasets is  
311 extremely challenging due to high collection costs and data management difficulties associated with the  
312 extremely large size of LIDAR datasets [Burian et al., 2006; Ching et al., 2009].

313 Observations from satellites, on the other hand, have been utilized in model validation  
314 processes over urban areas [Miao et al., 2009; Giannaros et al., 2013]. In addition to in situ observations,  
315 Giannaros et al. [2013] included MODIS (Moderate Resolution Imaging Spectroradiometer) based Land  
316 Surface Temperature (LST) products in their modeling study of the urban heat island (UHI) over Athens,  
317 Greece. Similarly, Miao et al. [2009] utilized 1-km-resolution MODIS data to verify the WRF-Noah-UCM

Deleted: Taha

319 simulated LST distribution in Beijing. Other studies have employed satellite data to replace outdated  
320 urban land use maps in atmospheric models with new remote sensing products [Cheng and Byun, 2008;  
321 Cheng et al., 2013]. Focusing on boundary layer mixing conditions and local wind patterns in the  
322 Houston Ship channel, Cheng and Byun [2008] reported that the Noah LSM and planetary boundary  
323 layer (PBL) scheme performances in the MM5 were improved when land-use type distributions were  
324 correctly represented in the model using high resolution Landsat-based land use data. Cheng et al.  
325 [2013] compared WRF simulations in the Taiwan area using U.S. Geological Survey (USGS), MODIS, and  
326 SPOT (Système Pour l'Observation de la Terre) based land use data. Using the new high resolution land  
327 use types obtained from SPOT satellite imagery, the WRF predictions of daytime temperatures and  
328 onshore sea breezes had the best agreement with observed data. Furthermore, more accurate surface  
329 wind speeds were simulated when MODIS and SPOT data replaced conventional USGS land use maps in  
330 the WRF runs due to the more realistic representation of roughness length in the remotely sensed  
331 databases. Although these and other previous studies [e.g., Jin and Shepherd, 2005] have recognized the  
332 usefulness of satellite imagery (e.g., NASA's Terra, Aqua, and Landsat data) in specifying surface physical  
333 characteristics in urban environments, very few have directly incorporated high resolution gridded  
334 satellite-based parameters (e.g., impervious surface area, albedo, and emissivity) into parameter  
335 estimation within land surface/atmospheric modeling systems.

336 In the current work we investigate the utility of remote sensing based surface parameters in the  
337 Noah-UCM modeling framework over a highly developed urban area. Among parameters that can be  
338 related to a measurable physical quantity, we evaluate those routinely and freely obtained from  
339 satellite-based platforms. The derived parameter sets are implemented in the Noah-UCM with a focus  
340 on simulated surface energy and water cycles that are essential feedback to the widely used WRF  
341 model. Landsat and fused Landsat-MODIS data are utilized to generate high resolution (30 m) monthly  
342 spatial maps of green vegetation fraction (GVF), impervious surface area (ISA), albedo, leaf area index

Deleted: later

344 (LAI), and emissivity in the Los Angeles metropolitan area. The temporal and spatial distributions of  
345 newly assigned parameters are compared with those based on the model lookup tables. Next, gridded  
346 remotely sensed parameter datasets are directly incorporated into the Noah-UCM modeling framework  
347 replacing the land-use/lookup-table-based values. The sensitivity of the simulated energy and water  
348 fluxes to the newly developed spatial metrics of parameters is presented. The model's performance in  
349 reproducing evapotranspiration (ET) and LST fields is evaluated utilizing Landsat-based land surface  
350 temperature and ET estimates from CIMIS (California Irrigation Management Information System)  
351 stations as well as in-situ measurements. Finally, the influence of each parameter set on the urban  
352 energy and water budgets is investigated.

353

## 354 **2. Study Area**

355 The study domain is a 49 km<sup>2</sup> highly developed neighborhood in the City of Los Angeles (Fig. 1). Los  
356 Angeles is the second most populous city in the United States with a population of 3.8 million [U.S.  
357 Census, 2011], covering an area of 1,215 km<sup>2</sup> in Southern California. The City has a Mediterranean  
358 climate and receives 381 mm of annual precipitation, mostly over the winter months [NOAA-CSC, 2003;  
359 SCDWR, 2009]. Due to the semi-arid nature of the region, the City's water supply is heavily dependent  
360 on imported water (52% from the Colorado River and 36% from the Los Angeles Aqueduct) [LADWP,  
361 2010]. Regional water demands and the extensive dependence on external sources make accurate  
362 spatial representation of the metropolitan area in regional land surface/atmospheric models imperative  
363 for predicting current and future water budgets. The study domain includes commercial/industrial as  
364 well as low and high intensity residential land cover types and a large park with both irrigated and non-  
365 irrigated landscapes (Fig. 1b and 1c).

366

367

### 368 3. Remotely Sensed Parameters

369 Remote sensing data are retrieved from Landsat ETM+ images with a nominal pixel resolution of 30 m in  
370 the short wave bands and 60 m in the thermal band. The level 1Gt ETM+ imagery from USGS EROS,  
371 spanning years 2010-2011, are calibrated and atmospherically corrected through the Landsat Ecosystem  
372 Disturbance Adaptive Processing System (LEDAPS). Study domain data are not affected by the failure of  
373 the Landsat-7 ETM+ Scan Line Corrector in [2003](#) (SLC-off). Employing a knowledge-based approach,  
374 similar to the one introduced by Song and Civco [2002], several binary masks are applied to the images  
375 to detect contaminated areas (cloud and shadow). Images with cloud and/or shadow are distinguished  
376 and omitted in the following parameter retrievals. A total of 24 pure images, acquired over two years,  
377 are utilized in the parameter estimation processes.

378 In addition to Landsat observations, MODIS products from Terra and Aqua satellite platforms  
379 are also utilized. The MODIS MCD43A BRDF (Bidirectional Reflectance Distribution Function) products,  
380 concurrent with pure Landsat images, are collected for use in the parameter calculations. The 500-m  
381 BRDF products are generated by the MODIS Adaptive Processing System (MODAPS) at the Goddard  
382 Space Flight Center (GSFC), using a kernel-driven linear model, and distributed through the Land  
383 Processes DAAC (Distributed Active Archive Center) [Justice et al., 2002; Schaaf et al., 2002; Shuai et al.,  
384 2008]. The described Landsat and MODIS-based data are used to produce a group of six remotely sensed  
385 derivatives:

- 386 • *Green Vegetation Fraction (GVF)*: GVF spatial maps are derived according to Gutman and  
387 Ignatov [1998] utilizing NDVI (Normalized Difference Vegetation Index) measurements. First,  
388 atmospheric corrected reflectance values from the red ( $\rho_{ETM3}$ ) and near-infrared ( $\rho_{ETM4}$ ) bands of Landsat  
389 ETM+ are used to derive NDVI maps for each date of imagery based on Eq. 1. Next, assuming the  
390 vegetated part of a pixel is covered by dense vegetations (i.e., it has a high LAI), GVF is calculated using  
391 Eq. 2.

Deleted: 2033



393 
$$NDVI = \frac{\rho_{ETM4} - \rho_{ETM3}}{\rho_{ETM4} + \rho_{ETM3}} \quad \text{Eq. (1)}$$

394 
$$GVF = \frac{NDVI - NDVI_0}{NDVI_{\infty} - NDVI_0} \quad \text{Eq. (2)}$$

395 Where  $NDVI_0$  and  $NDVI_{\infty}$  are constant values computed using signals from bare soil and densely  
396 vegetated pixels in the study domain, respectively.

397 • *Impervious Surface Area (ISA)*: ISA is shown to be inversely proportional to vegetation fraction  
398 where non-vegetated pervious surfaces are rare [Bauer et al., 2007]. Since the majority of pervious  
399 surfaces in the studied domain are vegetated and heavily irrigated throughout the year, ISA is assumed  
400 to be the complement of the vegetation fraction:

401 
$$ISA = (1 - GVF_{max}) \cdot 100 \quad \text{Eq. (3)}$$

402 Where  $GVF_{max}$  is the maximum GVF detected over the two year study period. The produced ISA map  
403 shows high accuracy (>95%) when compared to a previously developed high resolution land cover map,  
404 based on QuickBird remote sensing data, aerial photographs, and geographic information systems over  
405 the city of Los Angeles [McPherson et al., 2008]. We speculate that one cause contributing to the high  
406 accuracy of this assumption is that ISA overestimation, induced by non-vegetated pervious surfaces, is  
407 offset by tree canopies that cover areas larger than underlying pervious surfaces.

Deleted: that may contribute

408 • *Albedo*: Employing a recent methodology by Shuai et al. [2011], 30 m land surface albedo maps  
409 is generated utilizing Landsat surface reflectance and anisotropy information from concurrent 500 m  
410 MODIS BRDF products. Landsat data are reprojected from UTM to MODIS sinusoidal projection and  
411 aggregated from 30 m to 500 m. Using USGS-based land cover types, the percentage of each land cover  
412 class within each MODIS pixel is computed, then relatively pure pixels (>85% purity) are selected for  
413 each class. MCD43A2 quality assessment product is used to choose highest quality MODIS MCD43A1

415 BRDF parameters for the pure pixels. The concurrent parameters are used to calculate nadir  
 416 reflectance, white sky albedo, and black sky albedo under the solar geometry at Landsat overpass time  
 417 and MODIS scale. Next, the spectral albedo-to-nadir reflectance ratios, for white sky and black sky  
 418 albedos, are calculated over the pure pixels. The resultant ratios, specific to each land cover class, are  
 419 applied to Landsat surface reflectance to generate the spectral white sky and black sky albedos for each  
 420 Landsat pixel. A further narrowband-to-broadband conversion based on extensive radiative transfer  
 421 simulations by Liang [2000] is applied to generate the broadband albedos at shortwave regime. Finally,  
 422 albedo (blue sky) is modeled as an interpolation between the black sky ( $\alpha_{bs}$ ) and white sky ( $\alpha_{ws}$ ) albedos  
 423 as a function of the fraction of diffuse skylight ( $S(\theta, \tau(\lambda))$ ) which is estimated by the 6S (Second Simulation  
 424 of the Satellite Signal in the Solar Spectrum) codebase (Eq. 4) [Schaaf et al., 2002].

$$425 \quad \alpha(\theta, \lambda) = \{1 - S(\theta, \tau(\lambda))\} \alpha_{bs}(\theta, \lambda) + S(\theta, \tau(\lambda)) \alpha_{ws}(\theta, \lambda) \quad \text{Eq. (4)}$$

426 where  $\tau$ ,  $\theta$ , and  $\lambda$  are optical depth, solar zenith, and wavelength, respectively.

427 • *Leaf Area Index (LAI)*: Stenberg et al. [2004] showed that a reduced simple ratio (RSR) explains  
 428 63%-75% of the variations in LAI and that maps of projected LAI, based on RSR, have good agreement  
 429 with observations. In the current study, LAI values are retrieved based on the LAI-RSR correlations which  
 430 are specified utilizing table-based LAI estimates in pure (fully vegetated) pixels and remotely sensed RSR  
 431 maps. The atmospheric corrected reflectance values of Landsat ETM spectral channels red ( $\rho_{ETM3}$ ), near  
 432 infrared ( $\rho_{ETM4}$ ), and mid infrared ( $\rho_{ETM5}$ ), implemented in the following equation (Eq. 5), define RSR:

$$433 \quad RSR = \frac{\rho_{ETM4}}{\rho_{ETM3}} \cdot \frac{\rho_{5max} - \rho_{ETM5}}{\rho_{5max} + \rho_{5min}} \quad \text{Eq. (5)}$$

434 where  $\rho_{ETM5min}$  and  $\rho_{ETM5max}$  are the smallest and largest mid infrared reflectance detected in the Landsat  
 435 ETM images over the study domain, excluding open water pixels.

436 • *Emissivity*: Among various methods developed to define land surface emissivity, the NDVI  
 437 Thresholds Method (NDVI<sup>THM</sup>) has been widely applied to urban areas [Stathopoulou and Cartalis, 2007;  
 438 Stathopoulou et al., 2007; Tan and Li, 2013]. NDVI<sup>THM</sup> is superior to other methods since the  
 439 consideration of the internal reflections (cavity effects), caused by heterogeneous surfaces minimizes  
 440 the overall error in this approach [Sobrino et al., 2001]. This methodology, originally introduced by  
 441 Sobrino and Raissouni [2000] and modified later by Stathopoulou et al. [2007] for urban areas, is  
 442 selected for land surface emissivity estimation in the current work. Using the Landsat-based NDVI  
 443 thresholds, the study area is divided into four classes: (1) fully vegetated (NDVI>0.5), (2) built-up areas  
 444 with sparse vegetation (NDVI≤0.2), (3) mixture of man-made material and vegetation (NDVI>0.2 and  
 445 ≤0.5), and (4) water bodies (NDVI<0). Mean emissivity values of 0.980, 0.920, and 0.995 are then used  
 446 for fully vegetated, built-up and water pixels [Similar to Tan and Li, 2013]. Emissivity values (ε) for mixed  
 447 pixels (class 3) are estimated using the following equations [for details see Stathopoulou et al., 2007]:

$$\varepsilon = 0.017P_V + 0.963 \quad \text{Eq. (6)}$$

$$P_V = \frac{(NDVI-0.2)^2}{(0.5-0.2)^2} \quad \text{Eq. (7)}$$

450 • *Land Surface Temperature (LST)*: The emissivity corrected land surface temperature (LST) is  
 451 calculated as follows [Artis & Carnahan, 1982]:

$$LST = \frac{BT}{\left\{1 + \left[\frac{\lambda BT}{\rho} \cdot \ln \varepsilon\right]\right\}} \quad \text{Eq. (8)}$$

453 where BT is Landsat at sensor brightness temperature (K); λ and ε are the wavelength of emitted  
 454 radiance (11.5 μm) and surface emissivity; ρ = hc/σ (1.438 × 10<sup>-2</sup> m K); σ, h, and c are Boltzmann  
 455 constant, Planck's constant, and the velocity of light, respectively.

456

457 **4. Numerical Modeling System**

458 **4.1. Noah LSM-UCM Model**

459 Land surface processes are parameterized using the offline Noah LSM [Chen and Dudhia, 2001] coupled  
460 with the single layer UCM [Kusaka et al. 2001; Kusaka and Kimura, 2004]. The Noah LSM is based on a  
461 diurnally dependant Penman potential evaporation approach, a multi-layer soil parameterization, a  
462 canopy resistance model, surface hydrology, and frozen ground physics [Chen et al., 1996, 1997; Chen  
463 and Dudhia, 2001; Ek et al., 2003]. The UCM parameterization includes urban building geometry,  
464 shadowing from buildings, reflections and trapping of radiation in a street canyon, and an exponential  
465 wind profile. The Noah LSM provides surface sensible and latent heat fluxes and surface skin  
466 temperature for vegetated areas (e.g., parks and trees) and the UCM calculates the fluxes for  
467 impervious surfaces. The outputs from the Noah LSM and UCM are coupled through the urban surface  
468 fractions.

469 **4.2. Irrigation Module**

470 Irrigation is accounted for, in the Noah-UCM modeling framework, by incorporating an urban irrigation  
471 module developed in our previous work [Vahmani and Hogue, 2013; 2014]. The developed irrigation  
472 scheme mimics the effects of urban irrigation by increasing soil moisture content in vegetated portion of  
473 grid pixels at a selected interval. Added anthropogenic soil moisture contribution is a function of the soil  
474 moisture deficit, which is the difference between irrigated soil moisture content and actual soil moisture  
475 content in the top soil layer. The irrigation module calculates irrigated soil moisture content ( $SMC_{IRR}$ ;  $m^3$   
476  $m^{-3}$ ), soil moisture deficit (DEF;  $m^3 m^{-3}$ ), and irrigation water (IRR;  $kg m^{-2} s^{-1}$ ) as:

477 
$$SMC_{IRR} = \alpha \cdot SMC_{max} \quad \text{Eq. (9)}$$

478 
$$DEF = \max\{[SMC_{IRR} - SMC_1], 0\} \quad \text{Eq. (10)}$$

479 
$$IRR = \frac{\rho_w}{\Delta t} DEF \cdot D_1 \quad \text{Eq. (11)}$$

480 where saturation soil moisture content ( $SMC_{max}$ ;  $m^3 m^{-3}$ ) and irrigation demand factor ( $\alpha$ ; unit less)  
481 define irrigated soil moisture content (Eq. 9);  $D_1$  is top soil layer thickness (10 cm);  $\rho_w$  ( $kg m^{-3}$ ) and  $\Delta t$   
482 stand for water density and Noah-UCM time step (3600 s), respectively. The parameter  $\alpha$ , ranging from  
483 zero to one, regulates the amount of irrigation water added to the soil each time the scheme increases  
484 the soil moisture, simulating an irrigation event. Similar to previous studies [Hanasaki et al. 2008a,  
485 2008b; Pokhrel et al. 2012] an irrigation demand factor of 0.75 is utilized in the current work. The  
486 irrigation interval is set to three times per week according to the water restrictions implemented by Los  
487 Angeles Department of Water and Power (LADWP) in 2010 (LADWP, personal communication, 2013).

#### 488 4.3. Improving the UCM-simulated LST

Deleted: 4.3.

489 The calculation of the impervious surface temperature in the UCM version used in this study has been  
490 shown to be inaccurate [Li and Bou-Zeid, 2014]. This is due to the fact that the turbulent transfer  
491 coefficient ( $C_h$ ) for the whole pixel is calculated using only momentum and thermal roughness lengths of  
492 vegetated portion, ignoring the developed surface impact on  $C_h$ . Li and Bou-Zeid [2014] showed that this  
493 inconsistency could result in large biases in simulated LST values. In the current study, an alternative LST  
494 calculation, proposed by Li and Bou-Zeid [2014], is used as follows. First, a revised surface temperature  
495 of the impervious part of the pixel ( $T_s$ ) is calculated based on canyon temperature ( $T_c$ ) and roof surface  
496 temperature ( $T_r$ ):

$$497 T_s = f_r \times T_r + (1 - f_r) \times T_c \text{----- Eq. (12)}$$

498 where  $f_r$  is the roof fraction of the impervious surface. Note that the  $T_c$  calculated by the UCM is an  
499 equivalent aerodynamic surface temperature aggregated for canyon surfaces, including walls and roads.  
500 Next, the LST for the whole grid cell is computed as a weighted average based on the  $T_s$  and surface  
501 temperature of pervious part ( $T_1$ ):

$$502 LST = f_{urb} \times T_s + (1 - f_{urb}) \times T_1 \text{----- Eq. (13)}$$

503 where  $f_{urb}$  is the urban fraction of the pixel.

#### 505 **4.4. Land Cover Data and Forcing Fields**

506 The Noah-UCM modeling system requires static data to describe physical characteristics of the surface,  
507 including soil type, slope type, vegetation type, and urban type. A combination of the Soil Data Mart  
508 [<http://soildatamart.nrcs.usda.gov>] and the Los Angeles Department of Public Works (LADPW)  
509 databases are used to gather soil classification information. Land use and land cover are parameterized  
510 using the 30 m NOAA C-CAP-2006 land cover data which is transformed to urban and vegetation type  
511 spatial maps over the study domain. High, medium, and low intensity developed land cover types,  
512 recognized by NOAA, are converted to UCM Industrial/Commercial, high and low intensity residential  
513 types, respectively. The developed open space along with natural land types are categorized as one of  
514 the 27 Noah LSM vegetation classes.

515 The offline Noah LSM-UCM is forced utilizing hourly ground-based observations from CIMIS and  
516 National Climatic Data Center (NCDC) stations for the period from 1 January 2010 to 31 December 2011.  
517 There are ten CIMIS and eight NCDC stations within close proximity of the study domain (Figure 1a). The  
518 NCDC stations, which use Automated Surface Observing Systems (ASOS), are located at smaller local  
519 airports (6 stations), one major airport (Los Angeles International Airport), and a university campus  
520 (University of Southern California; USC) within the Los Angeles metropolitan area. Reporting the  
521 meteorological conditions, the NCDC stations are used for wind speed, air temperature, relative  
522 humidity, air pressure, and incoming long wave radiation. All NCDC data are gathered at a standard  
523 reference height of 2m. The regional CIMIS stations are utilized for solar radiation (using LI2005  
524 pyranometer) and tipping bucket rain gauges in 18 stations (NCDC and CIMIS) are included in collection  
525 of precipitation data. Inverse-distance weighting (2<sup>nd</sup> power) is employed to create the spatial gridded  
526 forcing fields. Linear interpolation and data from the nearest gage are utilized to replace missing data.

527

#### 528 **5. Numerical Experiments and Evaluation Methods**

529 **5.1. Remote Sensing Based Parameterization**

530 To investigate the sensitivity of the Noah-UCM model to integration of the developed remotely sensed  
531 parameters, nine simulation scenarios are designed (Table 1). A control experiment (Scenario 1) is  
532 conducted in which all default parameters are utilized in the Noah-UCM. Scenarios 2 to 6 explicitly  
533 assess each individual parameter effects on urban energy and water budgets using the newly  
534 incorporated remote sensing parameters. Scenario 7 analyzes the effects of employing both remotely  
535 sensed GVF and ISA while Scenario 8 assesses simultaneous integration of albedo, LAI, and emissivity.  
536 We are interested in the comparison of Scenarios 7 and 8 as the Noah-UCM parameterizations use GVF  
537 and ISA to select albedo, LAI, emissivity, and roughness length values from the predefined ranges in the  
538 parameter tables. It is worth mentioning that GVF alters the roughness length values over pervious or  
539 natural areas. However, roughness length and building height over the impervious surfaces are kept at  
540 the default values listed by Chen et al. [2011]. Scenarios 7 and 8 help quantify the contribution of each  
541 parameter group to the model's ability to reproduce the observed surface states and fluxes. Finally, the  
542 last experiment (Scenario 9) implements all five remotely sensed parameter sets in the simulations. It  
543 should be noted that the GVF and LAI measurements over mixed pixels (vegetated urban areas) are  
544 scaled up by multiplying the remotely sensed values by  $1/(1-\text{urban fraction})$  since in the Noah-UCM  
545 modeling framework these parameters characterize only the pervious portion (1 - urban fraction) of  
546 each pixel. However, remotely sensed albedo and emissivity values over each pixel are assigned to both  
547 pervious and impervious surfaces for that pixel. Other than the implemented remote sensing based  
548 parameters, the rest of the model parameters are kept at default values. All experiments incorporate  
549 the irrigation module and irrigation rates are kept constant in all scenarios. All scenarios are run at 30 m  
550 spatial and 1 hour temporal resolutions, spanning 2010 and 2011, with the first three months used as  
551 model initialization.

552 **5.2. Model Evaluation Approach**

Deleted: using urban fractions

Deleted: ,

Deleted: ,

Deleted: sending

557 In order to evaluate the performance of the Noah-UCM modeling framework, simulated LSTs are  
558 compared with concurrent Landsat observations and simulated latent heat flux time series are assessed  
559 against CIMIS-based ET observations. The CIMIS network was established in 1982 by the CDWR  
560 (California Department of Water Resources) and the University of California at Davis in order to provide  
561 real-time weather conditions and irrigation water need estimates for California's agricultural  
562 community. The automated CIMIS stations measure hourly surface solar radiation, temperature,  
563 humidity, wind, precipitation, soil temperature, and surface pressure [http://www.cimis.water.ca.gov].  
564 Employing observed meteorological fields over a well-watered soil, the reference ET ( $ET_0$ ) is calculated  
565 for each site. Utilizing a methodology introduced by CDWR [2000], actual urban landscape ET is  
566 estimated using  $ET_0$  and a landscape coefficient, which is a function of species, density, and  
567 microclimate factors. Based on the authors' knowledge in the study landscape as well as a report by  
568 CDWR [2000], we assume "Moderate" (trees and shrubs) and "High" (turf grass) water needs. Following  
569 the CDWR [2002] instructions on irrigation zones with mixed water need categories (i.e., low, moderate,  
570 and high), a value from high category is selected (average species factor=0.80). Assuming the "average"  
571 category for vegetation density, a density factor of 1 is used. Furthermore, a "high" category of  
572 microclimate condition is used (microclimate factor=1.25) for the current highly developed study  
573 domain. This factor is utilized to take into account the contribution of the developed surfaces to the  
574 water loss from vegetated areas, through anthropogenic heating, reflected light, and high temperatures  
575 of surrounding heat-absorbing surfaces (e.g., paving and buildings). Using these factors, a landscape  
576 coefficient of 1 (landscape coefficient = species factor  $\times$  density factor  $\times$  microclimate factor) is  
577 prescribed. This coefficient and  $ET_0$  estimations from ten CIMIS stations within close proximity of the  
578 study domain (Fig. 1a) are utilized to compute the urban landscape ET. Inverse-distance weighting (2<sup>nd</sup>  
579 power) is employed to create spatial gridded ET maps over fully vegetated pixels in the study area which  
580 is then used in validation processes of the Noah-UCM. ET output of the model is also evaluated against

Deleted: /cimis



582 recent ET measurements in the greater Los Angeles area [Moering, 2011]. Moering [2011] employed a  
583 previously developed chamber approach to measure instantaneous ET in an irrigated and a non-  
584 irrigated park in the Los Angeles metropolitan area during WY (Water Year) 2011 (WY is defined as Oct.  
585 1st of the previous year to Sep. 30th of the designated year). They reported an annual ET of about 1224  
586 mm over the observed irrigated park, which is located within our study domain.

587

## 588 **6. Sensitivity Study of Surface Parameters**

### 589 **6.1. Temporal Evaluation**

590 The monthly time series of the default Noah-UCM and remote sensing based GVF, ISA, albedo, and LAI  
591 are compared and modeled cumulative monthly sensible and latent heat fluxes, using default and newly  
592 estimated parameters, are presented over fully vegetated, low intensity residential, and  
593 industrial/commercial areas (Fig. 2). Fluxes from high intensity residential areas are not presented as  
594 they behave similarly to those from the industrial/commercial areas. Except for the summer months,  
595 GVF values are significantly increased throughout the year when remote sensing products are utilized  
596 (Fig. 2a). Moreover, the default seasonal variations of GVF values, assumed over all the land cover types,  
597 are not detected in Landsat imagery (Fig. 2a). The reason for this is the significant and year round  
598 irrigation in the Los Angeles area, which is not accounted for in the default parameter tables. This is  
599 confirmed by previous studies [Johnson and Belitz, 2012] that reported urban vegetation supported by  
600 water delivery, in contrast to common seasonal behavior of greening in the winter/spring and browning  
601 in the summer, maintains constant greenness which is reflected in NDVI and GVF estimates. GVF plays a  
602 dominant role in the Noah-UCM simulations as it defines the vegetated fraction of the natural areas,  
603 and specifies albedo, LAI, emissivity, and roughness length values from the predefined ranges in the  
604 model lookup tables. Furthermore, GVF partitions the total ET between soil direct and canopy ET. The  
605 simulated latent heat flux is considerably decreased (up to 139 MJ m<sup>-2</sup> per month) in the summer time

606 and increased over the remaining months, when remotely sensed GVF is incorporated in the fully  
607 vegetated areas (Fig. 2b). Since any increase of latent heat flux that does not alter the radiative balance  
608 leads to a reduction in sensible flux, the newly developed GVF values, in turn, cause enhancements (up  
609 to  $103 \text{ MJ m}^{-2}$  per month) in the simulated summer sensible heat fluxes and a reduction in the sensible  
610 heat fluxes during the remaining months (Fig. 2b). Latent and sensible heat fluxes from the low intensity  
611 residential pixels show similar but less significant changes (up to  $66.1$  and  $31.0 \text{ MJ m}^{-2}$  per month,  
612 respectively), when the new parameter sets are implemented. Adding remotely sensed GVF causes  
613 insignificant changes in the industrial/commercial area fluxes due to the small percentage of vegetated  
614 land cover in such areas (Fig. 2d).

615 There are also large deviations between the look-up-table-based ISAs and the remotely sensed  
616 values. Averaged ISA is decreased (10%) over industrial and commercial pixels and increased (49%) over  
617 low intensity residential areas, when remote sensing products are utilized in the parameter estimation  
618 process (Fig. 2.e). These changes in the impervious surface area, or urban fraction values, have  
619 significant effects on monthly latent and sensible heat fluxes over the developed pixels (Fig. 2g and 2h),  
620 due to the critical role of urban fraction in partitioning of the energy fluxes. Over the low intensity  
621 residential areas, higher ISA values minimize the effects of urban vegetation which leads to latent heat  
622 fluxes decreases (up to  $62.6 \text{ MJ m}^{-2}$  per month) and sensible heat fluxes increases (up to  $52.4 \text{ MJ m}^{-2}$  per  
623 month), throughout the year, when remotely sensed data replace default urban fractions (Fig. 2g).  
624 These changes are reversed and less significant over the industrial and commercial pixels (maximum  
625 latent and sensible heat flux changes of  $30.0$  and  $26.5 \text{ MJ m}^{-2}$  per month, respectively; Fig. 2h). ISA has  
626 no influence on the fluxes from fully vegetated pixels which do not include impervious areas (Fig. 2.f).

627 Considerable changes in the monthly albedo averages are detected when incorporating remote  
628 sensing data in the parameterization process (Fig. 2i). Using fused Landsat and ~~MODIS~~ products, a  
629 reduction of averaged albedo values is observed over the fully vegetated and residential areas (up to

Deleted: MODIS

631 48% and 39%, respectively; Fig. 2i). Moreover, the default seasonal variations are hardly noticeable in  
632 the remote sensing based albedo values, which is due to the consistent greenness in the study area from  
633 irrigation throughout the year. On the other hand, considerable albedo increases (up to 39%) are  
634 detectable over the industrial/commercial pixels (Fig. 2i), which are caused by bright and highly  
635 reflective materials seen mainly over the rooftops of industrial/commercial buildings. Albedo affects the  
636 radiative energy budget and consequently available energy for the turbulent fluxes. In the current study,  
637 decreased albedo values over the fully vegetated and low intensity residential areas result in reduced  
638 loss of solar and long wave radiation respectively and, in turn, increases the sensible heat flux (up to  
639 33.8 and 21.5 MJ m<sup>-2</sup> per month; Fig. 2j and 2k). Albedo induced sensible heat decreases over  
640 industrial/commercial pixels are also noticeable (up to 33.9 MJ m<sup>-2</sup> per month; Fig. 2l).

641 Distinct seasonal fluctuations of LAI are observed in the remotely sensed data and the default parameter  
642 tables (Fig. 2m). This reflects the fact that landscape plantings are quite different from agricultural crops  
643 due to their being composed of collections of vegetation species and affected by complex irrigation  
644 patterns which are not taken into account in the vegetation parameter tables in the Noah LSM [CDWR,  
645 2000; Vahmani and Hogue, 2013; 2014]. Over the heavily vegetated pixels, the default pattern is  
646 reversed in the measured parameter sets with less seasonal variations and peaks in the winter time, due  
647 to the fact that most of the precipitation occurs in the winter months, over the current study domain  
648 (Fig. 2m). The industrial and commercial pixels illustrate higher LAI values in the remotely sensed  
649 parameter maps, year round, when compared to the default values (Fig. 2m). LAI is a critical parameter  
650 in the Noah LSM, which is involved in the parameterization of the canopy resistance, controlling canopy  
651 ET rates. In the presented results (Figs. 2n and 2o), LAI induced changes in the simulated turbulent fluxes  
652 are more apparent in the summer months and over fully vegetated and residential pixels, where  
653 sensible heat flux is significantly increased (up to 57.2 and 86.5 MJ m<sup>-2</sup> per month, respectively) and  
654 latent heat flux is significantly decreased (up to 65.5 and 97.9 MJ m<sup>-2</sup> per month, respectively). This is

655 due to the considerable decreases in the LAI values in summer time which lead to elevations of the  
656 canopy resistance and therefore reductions of the transpiration from the vegetation, causing decreases  
657 in latent heat fluxes. This in turn partitions the net radiation more into sensible heat fluxes. LAI does not  
658 affect fluxes from industrial/commercial pixels with small pervious fractions (Fig. 2p). It is worth  
659 mentioning that changes in the turbulent fluxes time series, in particular the latent heat flux decreases  
660 in the summer months induced by implementation of satellite-based LAI, are to some extent captured in  
661 the simulations with the remote sensing based GVF (compare Fig. 2b with 2n and 2c with 2o). This  
662 reflects our previous point that GVF controls assigned LAI values to vegetated pixels in the Noah LSM  
663 and that realistic presentation of GVF in the modeling framework can enhance LAI inputs in the model  
664 when LAI measurements are not available.

665 Remotely sensed emissivity maps are also utilized to replace the default values in the Noah-  
666 UCM simulations, which results in changes in the emissivity values (up to 5.1%). However, the new  
667 surface parameterization leads to insignificant changes in turbulent fluxes (results now shown). The  
668 largest emissivity induced alterations in sensible heat fluxes are seen over industrial and commercial  
669 pixels (up to 31.2 MJ m<sup>-2</sup> per month). Latent heat fluxes are changed, the most significantly, over fully  
670 vegetated areas (up to 2.56 MJ m<sup>-2</sup> per month).

## 671 **6.2. Spatial Evaluation**

672 The spatial distributions of newly assigned GVF, ISA, albedo, and LAI are next compared with those  
673 based on the Noah-UCM lookup tables. Different urban surface parameterizations, along with their  
674 impacts on the simulated maps of turbulent sensible and latent heat fluxes, are presented (Fig. 3; Valid  
675 at 1100 LST on 14 April 2011). As expected, during the spring period (April), GVF values are significantly  
676 higher when remote sensing products are utilized, due to the irrigation effects which are ignored in the  
677 default parameters (Fig. 3a and 3b). Over fully vegetated and low intensity residential pixels, where a  
678 significant portion of the energy goes into evaporation and transpiration, latent heat flux increases

679 (about 300 and 230 W m<sup>-2</sup>, respectively) and sensible heat fluxes decreases (about 160 and 120 W m<sup>-2</sup>,  
680 respectively) are found (Fig. 3c and 3d) when utilizing the remote sensing GVF.  
681 The spatial distributions of ISA, or urban fraction, between the remote sensing and default values show  
682 similar patterns (Fig. 3e and 3f). However, industrial/commercial and high intensity residential areas are  
683 assigned noticeably higher urban fraction values in the remote sensing based maps (compare Fig. 3e and  
684 3f) which leads to lower latent heat fluxes (bias of up to about 130 W m<sup>-2</sup>) and higher sensible (bias of up  
685 to about 100 W m<sup>-2</sup>) in these pixels (Fig. 3g and 3h).

686 The Noah-UCM parameters, based on look-up tables, underestimate surface albedo values over  
687 highly urbanized pixels, when compared with remote sensing data (Fig. 3i and 3j). In particular, the  
688 industrial/commercial buildings with highly reflective rooftops are completely ignored. Over the highly  
689 vegetated areas, however, albedo values are slightly overestimated in look-up tables. Altering the  
690 energy budget, the newly developed albedo datasets lead to lower Noah-UCM-simulated sensible heat  
691 fluxes over intensely developed pixels (Fig. 3k). The sensible heat flux differences are only significant  
692 over industrial/commercial pixels which include buildings with bright roofs (up to ~300 W m<sup>-2</sup>). The  
693 changes in absolute surface albedos do not affect simulated latent heat fluxes as these reflective roofs  
694 are located in industrial/commercial areas with negligible pervious surfaces and simulated latent heat  
695 flux (Fig. 3l).

696 The remote sensing data detect higher LAI values over all pixel types, particularly over fully  
697 vegetated areas where new LAI values are significantly higher (Fig. 3m and 3n). By influencing the  
698 canopy resistance, these changes redefine the spatial distribution of turbulent fluxes (Fig. 3o and 3p).  
699 Over the densely vegetated areas, increases in latent heat flux (up to 50 W m<sup>-2</sup>) and decreases in  
700 sensible heat flux (up to 35 W m<sup>-2</sup>) are found (Fig. 3o and 3p). It is noteworthy that, as illustrated before  
701 (Fig. 3n and 3o), the most significant influences of LAI alterations are detected in the summer months.

**Deleted:** in the default parameterization.

**Deleted:** and higher fluxes over the vegetated areas

**Deleted:** the most

**Deleted:** ; Fig. 3k

**Deleted:** (Fig.

707 Thus, it is not surprising that the turbulent fluxes do not show significant sensitivity to the LAI changes in  
708 April.

709 Remotely sensed emissivity maps, implemented in the Noah-UCM simulations, show minimal  
710 effect on the output turbulent fluxes maps (results not shown). Our results (Fig. 2 and 3) agree with  
711 previous sensitivity studies performed with the Noah-UCM which indicated high sensitivity of the model  
712 to GVF, ISA, albedo, and LAI, and less model sensitivity to emissivity [Loridan et al., 2010; Wang et al.,  
713 2011]. Loridan et al. [2010] highlighted the critical role of ISA and LAI in the simulations of latent heat  
714 flux and albedo role in the sensible heat flux simulations. Investigating the peaks of diurnal turbulent  
715 fluxes, Wang et al. [2011] reported that latent heat flux is the most sensitive to the GVF. They also found  
716 that emissivity has minimal effects on the model outputs.

717

## 718 **7. Evaluation of Noah-UCM Performance**

719 After initial sensitivity tests, the model performance in reproducing ET and LST fields is evaluated using  
720 remotely sensed (independent from derived parameters) and in situ measurements. The comparisons of  
721 observed and simulated ET and LST, using different urban surface parameterizations (scenarios 1, 7, 8,  
722 and 9 in Table 1), are presented in figures 4, 5, and 6.

### 723 **7.1. ET Simulations**

724 The temporal variations of ET, simulated by the Noah-UCM model and averaged over fully vegetated  
725 pixels, are evaluated against CIMIS-based ET measurements, spanning 2010 and 2011 (Fig. 4). The  
726 presented observations are averages over fully vegetated pixels in the study domain, calculated using ET  
727 maps based on  $ET_0$  measurements from ten CIMIS stations, landscape coefficients, and inverse-distance  
728 weighting ( $2^{nd}$  power) (see section 5.2). The model reproduces similar ET behaviors when the default  
729 parameters and the second group of remotely sensed parameters (albedo, LAI, and Emissivity) are  
730 implemented (Fig. 4a and 4c). The ET differences between observations and the default simulation are

Deleted: 4).

732 minimal in the winter and fall months, due to the limited energy available for ET in those months. Over  
733 the warmer months, the observed and modeled ETs show distinct behaviors. CIMIS stations report two  
734 peaks, one in the spring and one in the summer time. Simulated ETs, however, illustrate one peak in the  
735 July. The Noah-UCM, using these parameterizations, underestimates ET rates for the most of winter and  
736 spring months and overestimates them in the summer time (Fig. 4a and 4c). Including remotely sensed  
737 albedo, LAI, and emissivity does not change the general seasonal pattern deviations of ET (Fig. 4a and  
738 4c), but it reduces the biases considerably (with  $R^2=0.83$  and  $RMSE=14.32$  mm/month). We note that  
739 model improvement is mostly associated with inclusion of remotely-sensed LAI maps in the model since  
740 albedo and emissivity have minimal influence on latent heat fluxes from heavily vegetated pixels (see  
741 Fig. 2j).

742 The new GVF and ISA values alter ET seasonal fluctuations significantly in scenario 7 (Fig. 4b). In  
743 agreement with CIMIS observations, the model with inclusion of remotely sensed parameters results in  
744 significantly higher ET values in the warming months (Feb.-May) and lower ETs in the summer time.  
745 Noting that ISA has minimal effects over the fully vegetated pixels, one explanation for this pattern is  
746 that higher green vegetation fraction detected by Landsat in late winter and early spring, increases  
747 transpiration rates as soon as the required energy is available and lower measured GVFs in the summer  
748 time suppresses the transpiration rates, resulting in the lower ET values. These changes enhance the  
749 model performance significantly (with  $R^2=0.92$  and  $RMSE= 11.77$  mm/month).

750 Including all the measured parameter sets (Fig. 4d), reduces the behavioral disagreements  
751 between observed and modeled monthly ET ( $R^2=0.86$ ). Large biases over the summer months are also  
752 reduced. However, ET values are overestimated over the rest of the year ( $RMSE=17.49$  mm/month).  
753 Although each newly developed parameter group enhances the model performance in predicting ET, the  
754 advantages are countered when all of the parameters are implemented in the model. This is possibly  
755 due to the complex interactions between the parameters (e.g. GVF and LAI) in the model structure.

756 A notable pattern detected by CIMIS data is the drop in ET values over the month of June. The sudden  
757 decrease in ET corresponds to the June Gloom weather pattern in southern California, when onshore  
758 flows result in persistent overcast skies with cool temperatures, as well as fog and drizzle in late spring  
759 and early summer [NWS, 2011]. The June Gloom effects are captured in scenarios 7 and 9 (Fig. 4b and  
760 4d) and not seen in scenarios 1 and 8 (Fig. 4a and 4c). Since ISA has minimal influence on ET from the  
761 fully vegetated pixels and the second group fails to simulate June Gloom influence, the improvements in  
762 scenarios 7 and 9, in capturing this phenomenon, are associated with a more accurate representation of  
763 GVF.

## 764 7.2. LST Simulations

765 In order to further evaluate model performance and examine the impacts of different remote sensing  
766 based parameter sets, Landsat-based LST measurements are utilized (Fig. 5 and 6). Statistics ( $R^2$  and  
767 RMSE) are also included to quantify the model performance using different urban surface  
768 parameterizations (Fig. 5). The observed LSTs, over fully vegetated pixels, are estimated with fair

769 accuracy by the default model ( $R^2=0.86$  and  $RMSE=3.21$  °C; Fig 5a). The model performance has almost  
770 the same level of accuracy over low intensity residential areas and is slightly worse (<1°C) over  
771 industrial/commercial pixels (Fig. 5e). Using remote sensing data over fully vegetated and low intensity  
772 residential pixels weakly improves the biases (with <1°C improvement; Fig. 5b-d and 5f-h). Over  
773 industrial/commercial areas, a systematic underestimation of the observed LST is identified ( $RMSE=3.96-$   
774  $4.59$ °C; Fig. 5i-l) which seems to be persistent after using different remotely sensed parameter sets. We  
775 speculate that this underestimation of LST over highly developed areas is due to lack of representation  
776 of anthropogenic heating in the current study.

777 A comparison of LST at 1100 LST on 14 April 2011 with four simulation cases is also presented  
778 (Fig. 6). Alterations due to use of remote sensing products are more noticeable in this spatial  
779 examination of the results. Using all the default parameters (scenario 1), observed LST is overestimated

**Deleted:** is slightly worse (~1°C)

**Deleted:**  $R^2=0.62$  and

**Deleted:** 6.15

**Deleted:** ). Both

**Deleted:** groups (scenarios 7 and 8) significantly improve the correlations between the observed and simulated LSTs (RMSE of 0.76 and 0.70, respectively; Fig. 5j and 5k). When all the parameters are used (scenario 9), the RMSE is enhanced to 0.82. However, the cold biases are persistent in all simulations, more significantly over

**Deleted:** surfaces (Fig. 5e-l).

**Deleted:** Further analysis (not shown here) indicates that underestimation of LST values is due to a fundamental problem in the UCM and cannot be immediately solved with available parameter choices. This problem is discussed in a related study investigating different schemes for LST and conductive heat fluxes in the UCM [Wang et al. 2011b]. Their study shows that the current UCM formulation results in a phase lag and cold biases in simulated surface temperature when compared to observations. The discussed cold biased could potentially be resolved utilizing a spatially-analytical scheme introduced by Wang et al. [2011b]. ¶



800 over the heavily vegetated areas and underestimated over highly developed pixels (Fig. 6a and 6b).  
801 Remotely sensed GVF and ISA (in scenario 7) significantly decrease LSTs over fully vegetated and low  
802 intensity residential pixels and increase temperatures over industrial and commercial areas, resulting in a  
803 better match with the observed LST map. The decreased simulated surface temperatures over heavily  
804 vegetated areas is due to higher GVF and consequently higher ET rates, which in turn lead to lower  
805 sensible heat flux and LSTs (see Fig. 3b). The increased LSTs over highly developed areas is likely due to  
806 lower GVF and higher ISA values detected in Landsat imagery, compared with the default values, which  
807 partition net radiation more into sensible heat flux (see Fig. 3b and 3f). The noticed changes in LST maps,  
808 using remotely sensed albedo, LAI, and emissivity (scenario 8), are small (compare Fig. 6a and 6e).  
809 Although simulated LSTs over fully vegetated areas are decreased, the observed temperatures are still  
810 overestimated (Fig. 6f). The LST decreases in scenario 8 may be explained by evaporative cooling effect  
811 of the higher LAI values over heavily vegetated areas (see Fig. 3n). Similar to scenario 7, considerable  
812 GVF induced LST reductions, over fully vegetated areas, improve the observed LST estimations in  
813 scenario 9 (Fig. 6h). Our assessment indicates that implemented satellite derived parameter maps,  
814 particularly GVF and ISA used in scenarios 7 and 9, enhance the Noah-UCM capability to reproduce the  
815 LST differences between fully vegetated pixels and highly developed areas (simulated LST differences of  
816 3.07, 6.78, 3.48, and 7.30 °C for scenarios 1, 7, 8, and 9 vs. observed LST difference of 11.25 °C).

**Deleted:** result

**Deleted:** However the model still underestimates the observed LSTs over the industrial and commercial pixels (Fig. 6b and 6e).

### 817 **7.3. Energy and Water Budget Evaluation**

818 Differences in the simulated energy and water budgets, with different surface parameterizations  
819 (scenarios 1, 7, 8, and 9 in the Table 1) are summarized for WY 2011 (Fig. 7). The emissivity induced  
820 changes to the energy and water budgets are insignificant and not included. The illustrated radiative and  
821 turbulent heat fluxes show that, unlike the longwave radiative fluxes, the simulated available solar  
822 radiations are altered considerably using different urban parameter sets (up to %6), particularly over  
823 fully vegetated (Fig. 7a) and industrial/commercial pixels (Fig. 7c). These changes are induced by new

**Deleted:** 1.31, 4.81, 1.55

**Deleted:** 4.93

**Deleted:** Nevertheless, the model still underestimates remotely sensed LST values, by about 9.91 °C for scenario 9, over the highly developed areas.

**Deleted:** Regardless of the parameterization processes, cold biases are persistent in all simulations, particularly over high intensity residential and industrial/commercial pixels (Fig. 6). As explained above, this underestimation of LST values is consistent with the literature and is reported to be due to a fundamental problem in the UCM which produces a phase lag and cold biases in simulated LST [Wang et al., 2011b]. ¶

839 surface albedo values utilized in scenarios 8 and 9. It is also observed that most of the incoming  
840 radiative energy is dissipated through latent heat fluxes, over heavily vegetated pixels (Fig. 7a and 7b),  
841 and sensible heat fluxes over industrial/commercial areas (Fig. 7c). These turbulent fluxes are also  
842 altered when different surface parameterizations are incorporated. Implementing all the remotely  
843 sensed parameters (scenario 9), the annual latent heat flux is increased (12%) over fully vegetated pixels  
844 (Fig. 7a), and the annual sensible heat flux is decreased (32%) over industrial/commercial pixels (Fig. 7c).  
845 Ground heat fluxes, however, are insignificant and unchanged.

846 Water budget terms also show variable behavior using different parameter sets over different  
847 land cover types (Fig. 7 d-f). Annual irrigation amounts exceed received precipitations over the pixels  
848 with significant vegetation fractions (Fig. 7d and 7e). This pattern is not rare in semi-arid regions [CDWR  
849 1975, Mini et al., 2014]. In these areas, most of incoming water is lost through ET (Fig. 7d and 7e). Areas  
850 with high coverage of impervious surfaces, however, dissipate most of the incoming moisture through  
851 surface runoff (Fig. 7f). The alterations in the annual ET rates are, for the most part, due to the changes  
852 in the GVF parameterizations (scenarios 7 and 9; Fig. 7d-f). Sub-surface runoff annual rates, on the other  
853 hand, are altered using new ISA values (scenarios 7 and 9; Fig. 7e and 7f). Changes in the annual ET  
854 values are as large as 145, 156, and 79.4 mm over fully vegetated, low intensity residential and  
855 industrial/commercial pixels, respectively (Fig. 7d-f).

856 To further verify the capability of Noah-UCM to reproduce observed ET quantities, additional  
857 evaluation of the model is conducted utilizing ground-based chamber ET measurements in the greater  
858 Los Angeles area [Moering, 2011]. Instantaneous ET measurements, over an irrigated park in the study  
859 domain during WY 2011, are converted to daily and then annual ET estimates (1224 mm) and compared  
860 with the simulated ET values over the parks (Fig. 7d). As expected, the observed ET is best reproduced  
861 by scenario 7 (Bias of 1.47 mm) due to more accurate representation of GVF in the model. Scenarios 1  
862 (with the default parameters) and 8 underestimate, with biases of 58.65 and 65.32 mm, respectively.

863 Scenario 9, with all the remotely sensed parameters, overestimates the measured ET (with bias of 86.24  
864 mm). These shortcomings are likely due to: (1) a lack of accurate representation of GVF in the default  
865 parameter sets, used in scenarios 1 and 8, (2) the uncertainties associated with the estimated LAI values  
866 utilized in scenarios 8 and 9, and (3) complex interactions between GVF and LAI noted in scenario 9.  
867 The presented analysis of energy balance (Fig. 7) suggests that GVF, albedo and LAI play an important  
868 role in regulating simulated radiative energy budget and turbulent fluxes, mainly by affecting the  
869 available net radiation and transpiration quantities. GVF, ISA, and LAI also alter the study area  
870 transpiration and ET values, as well as surface runoff rates.

871

## 872 **8. Conclusions**

873 In the current work we investigate the utility of a select set of remote sensing based surface parameters  
874 in the Noah-UCM modeling framework over a highly developed urban area. It was found that remote  
875 sensing data show significantly different magnitudes and seasonal patterns of GVF when compared with  
876 the default values. The reason for this mismatch is the significant and year round irrigation in the Los  
877 Angeles area which is not accounted for in the default parameter tables. Irrigated landscapes maintain  
878 constant greenness rather than a seasonal behavior of greening in the winter/spring and browning in  
879 the summer. The noticed differences between the monthly LAI values from default tables and remotely  
880 sensed data are also due to complex irrigation patterns. Another factor that contributes to this  
881 mismatch is the fact that landscape plantings are quite different from agricultural crops due to their  
882 being composed of collections of vegetation species which is not taken into account in the vegetation  
883 parameter tables in the Noah LSM [CDWR, 2000; Vahmani and Hogue, 2013; 2014]. There are also  
884 considerable deviations between the look-up-table-based ISA, albedo and emissivity maps and the  
885 remotely sensed values. The results of our analysis agree with previous studies which show high  
886 sensitivity of the Noah-UCM to GVF, ISA, albedo, and LAI, and minimal model sensitivity to emissivity

887 [Loridan et al., 2010; Wang et al., 2011]. Our results show that GVF, ISA and LAI are critical in the  
888 simulations of latent and sensible heat flux, and that albedo plays a key role in the sensible heat flux  
889 simulations.

890 Our assessment of the Noah-UCM ET estimation shows that using the default parameters leads  
891 to significant errors in the model predictions of monthly ET fields (RMSE= 22.06 mm/month) over the  
892 study domain in Los Angeles. Results show that accurate representation of GVF is critical to reproduce  
893 observed ET patterns over vegetated areas in the urban domains. LAI also plays an important role in ET  
894 simulations. However, simulations incorporating the remotely sensed GVF values outperform (RMSE=  
895 11.77 mm/month) simulations with the new LAI estimates (RMSE=14.32 mm/month). This could be due  
896 to several reasons. First, there are uncertainties associated with the remote sensing based LAI retrieval,  
897 including non-linearity of LAI-vegetation index (RSR) relationships [Latifi and Galos, 2010], which do not  
898 apply to NDVI-based GVF. Second, more accurate representation of GVF values in the Noah-UCM not  
899 only improves the assigned LAI values to the vegetated pixels in the model but also enhances other  
900 parameters inputs as well (i.e. albedo, emissivity, and roughness length). Further analysis of the model  
901 performance indicates that implemented satellite derived parameter maps, particularly GVF and ISA,  
902 enhance the Noah-UCM capability to reproduce the LST differences between fully vegetated pixels and  
903 highly developed areas (simulated LST differences of 3.07 and 6.78 °C for scenarios with default and  
904 remotely sensed GVF and ISA vs. observed LST difference of 11.25 °C).

905 Our analysis of energy balance suggests that GVF, albedo and LAI play an important role in  
906 regulating simulated radiative energy budget and turbulent fluxes, mainly by affecting the available net  
907 radiation and ET quantities. With regard to urban water balance, GVF, ISA, and LAI play a key role in  
908 surface hydrologic fluxes, including ET and surface runoff. When compared with in-situ observations,  
909 Noah-UCM shows the capacity to reproduce ET fields with relatively high accuracy (Bias of 1.47 mm)  
910 when GVF maps are updated using remote sensing data.

**Deleted:** 1.31

**Deleted:** 4.81

**Deleted:** Nevertheless, the model still underestimates remotely sensed LST values, over highly developed areas. We speculate that the underestimation of LST values, particularly over high intensity residential and industrial/commercial areas, is due to structural parameterization in the UCM and cannot be immediately solved with available parameter choices.

919 In summary, the current study highlights the significant deviations between the spatial distributions and  
920 seasonal fluctuations of the default and remotely sensed parameter sets in the Noah-UCM. We illustrate  
921 that replacing default parameters with the measured values reduces significant biases in model  
922 predictions of the surface fluxes within irrigated urban areas. This ultimately has key implications in  
923 feedback processes to the atmosphere when the Noah-UCM is coupled with the widely used WRF  
924 model, which has been increasingly applied over urban areas to examine the exchange of heat,  
925 moisture, momentum or pollutants. Semi-arid urban cities, [in particular](#), are receiving much attention in  
926 the literature, given their accelerated growth and increasing dependence on external water sources.  
927 More accurate representation of both water and energy fluxes [in commonly used modeling frameworks](#)  
928 is critical for regional resource management as well as predictions of urban processes under future  
929 climate conditions. [Although this study focuses on the widely used single layer UCM, we speculate that](#)  
930 [implementation of the more accurate remote sensing based parameters \(particularly, GVF and ISA\) may](#)  
931 [also enhance performance of the Noah-BEP \[Martilli et al., 2002\], which is currently the most](#)  
932 [sophisticated urban scheme in WRF. In this multi-layer UCM a similar approach to the single layer UCM](#)  
933 [is used based on an urban fraction \(or ISA\) parameter that couples the Noah outputs over pervious](#)  
934 [portion of pixels and UCM outputs over developed surfaces.](#)

### 935 **Acknowledgements**

936 Funding for this research was supported by an NSF Hydrologic Sciences Program CAREER Grant  
937 (#EAR0846662), a 2012 NASA Earth and Space Science Fellowship (#NNX12AN63H), and an NSF Water  
938 Sustainability and Climate (WSC) grant (#EAR12040235).

939

940 **References**

- 941 Arnfield, A. J.: Two decades of urban climate research: A review of turbulence, exchanges of energy and  
942 water, and the urban heat island, *Int. J. Climatol.*, 23: 1–26, doi: 10.1002/joc.859, 2003.
- 943 Artis, D. A. and Carnahan, W. H.: Survey of emissivity variability in thermography of urban areas, *Remote*  
944 *Sensing of Environment*, 12, 313–329, 1982.
- 945 Bauer, M. E., Loeffelholz, B., and Wilson, B.: Estimating and mapping impervious surface area by  
946 regression analysis of Landsat imagery, *Remote Sensing of Impervious Surfaces*, pp. 3–20, Boca Raton,  
947 Florida: CRC Press, 2007.
- 948 Bornstein, R.: Urban climate models: Nature, limitations, and applications, *Meteorol. Atmos. Phys.*, 38,  
949 185–194, 1987.
- 950 Burian, S. , Brown, M. J., Augustus, N.: Development and assessment of the second generation National  
951 Building Statistics database, Seventh Symposium on the Urban Environment, San Diego, CA, 10–13  
952 September, American Meteorological Society: Boston, MA, Paper 5.4, 2007.
- 953 Burian, S. J., Stetson, S. W., Han, W., Ching, J., and Byun, D.: High resolution dataset of urban canopy  
954 parameters for Houston, Texas, Preprint proceedings, Fifth Symposium on the Urban Environment,  
955 Vancouver, BC, Canada, 23–26 August, American Meteorological Society: Boston, MA, 2004.
- 956 Burian, S., Brown, M., McPherson, T. N., Hartman, J., Han, W., Jeyachandran, I., Rush, J.: Emerging urban  
957 databases for meteorological and dispersion, Sixth Symposium on the Urban Environment, Atlanta, GA,  
958 28 January–2 February, American Meteorological Society: Boston, MA, Paper 5.2, 2006.

Deleted: 9,

960 California Department of Water Resources (CDWR): A guide to estimating irrigation water needs of  
961 landscape plantings in California: The landscape coefficient method and WUCOLS III, [Department of](#)  
962 [Water resources](#), State of California, 1–150, 2000.

963 California Department of Water Resources (CDWR): California’s ground water, bulletin 118, [Department](#)  
964 [of Water resources](#), State of California, 1975.

965 Changnon, S. A. and Huff, F. A.: The urban-related nocturnal rainfall anomaly at St. Louis, *J. Climate Appl.*  
966 *Meteor.*, 25, 1985–1995, doi:[10.1175/1520-250450\(1986\)025<1985:TURNRA>2.0.CO;2](#), 1986.

967 Changnon, S. A.: Inadvertent weather modification in urban area: Lessons for global climate change.  
968 *Bull. Amer. Meteor. Soc.*, 73, 619–627, doi:[10.1175/1520-0477\(1992\)073<0619:IWMIUA>2.0.CO;2](#),  
969 1992.

970 Chen, F. and Dudhia, J.: Coupling an advanced land-surface/hydrology model with the Penn State/NCAR  
971 MM5 modeling system. Part I: model implementation and sensitivity, *Monthly Weather Review*, 129:  
972 569–585, 2001.

973 Chen, F., Janjic, Z., and Mitchell, K.: Impact of atmospheric surface layer parameterization in the new  
974 land-surface scheme of the NCEP mesoscale Eta model, *Boundary-Layer Meteorology*, 85: 391–421,  
975 DOI:[10.1023/A:1000531001463](#), 1997.

976 Chen, F., Kusaka, H., Bornstein, R., Ching, J., Grimmond, C. S. B., Grossman-Clarke, S., Loridan, T.,  
977 Manning, K. W., Martilli, A., Miao, S., Sailor, D., Salamanca, F. P., Taha, H., Tewari, M., Wang, X.,  
978 Wyszogrodzki, A. A., and Zhang, C.: The integrated WRF/urban modelling system: development,  
979 evaluation, and applications to urban environmental problems, *Int. J. Climatol.*, 31: 273–288. doi:  
980 [10.1002/joc.2158](#), 2011.

Deleted: <http://dx.doi.org/>

Deleted: <http://dx.doi.org/>

983 Chen, F., Kusaka, H., Tewari, M., Bao, J. W., Harakuchi, H.: Utilizing the coupled WRF/LSM/urban  
984 modeling system with detailed urban classification to simulate the urban heat island phenomena over  
985 the Greater Houston area, Paper 9.11, American Meteorological Society Fifth Symposium on the Urban  
986 Environment, Vancouver, BC, Canada, 2004.

987 Chen, F., Mitchell, K., Schaake, J., Xue, Y., Pan, H.-L., Koren, V., Duan, Q. Y., Ek, M., Betts, A.: Modeling of  
988 land-surface evaporation by four schemes and comparison with FIFE observations, *J. Geophys. Res.*,  
989 101(D3), 7251–7268, doi:10.1029/95JD02165, 1996.

990 Cheng, F. Y. and Byun, D.W.: Application of High Resolution Land Use and Land Cover Data for  
991 Atmospheric Modeling in the Houston-Galveston Metropolitan Area: Part I, *Meteorological Simulation*  
992 *Results, Atmospheric Environment*, 42, 7795-7811, doi:10.1016/j.atmosenv.2008.04.055, 2008.

993 Cheng, F. Y., Hsu, Y. C., Lin, P. L., Lin, T. H.: Investigation of the Effects of Different Land Use and Land  
994 Cover Patterns on Mesoscale Meteorological Simulations in the Taiwan Area, *J. Appl. Meteor. Climatol.*,  
995 52, 570–587, doi: <http://dx.doi.org/10.1175/JAMC-D-12-0109.1>, 2013.

996 Ching, J., Brown, M., McPherson, T., Burian, S., Chen, F., Cionco, R., Hanna, A., Hultgren, T., Sailor, D.,  
997 Taha, H., Williams, D.: National Urban Database and Access Portal Tool, NUDAPT, *Bulletin of the*  
998 *American Meteorological Society*, 90(8): 1157–1168, DOI:10.1175/2009BAMS2675.1, 2009.

999 Cotton, W. R. and Pielke, R. A.: *Human impacts on weather and climate*. Cambridge: Cambridge  
1000 University Press, 1995.

1001 De Ridder, K., Bertrand, C., Casanova, G., and Lefebvre, W.: Exploring a new method for the retrieval of  
1002 urban thermophysical properties using thermal infrared remote sensing and deterministic modeling, *J.*  
1003 *Geophys. Res.*, 117, D17108, doi:10.1029/2011JD017194, 2012.



1004 Ek, M. B., Mitchell, K. E., Lin, Y., Rogers, E., Grunmann, P., Koren, V., Gayno, G., Tarpley, J. D.:

1005 Implementation of Noah land surface model advances in the National Center for Environmental

1006 Prediction operational mesoscale Eta model, *J. Geophys. Res.*, 108, 8851, doi:10.1029/2002JD003296,

1007 2003.

1008 Giannaros, T. M., Melas, D., Daglis, I. A., Keramitsoglou, I., Kourtidis, K.: Numerical study of the urban

1009 heat island over Athens (Greece) with the WRF model, *Atmospheric Environment*, Volume 73, 103-111,

1010 doi:10.1016/j.atmosenv.2013.02.055, 2013.

1011 Gutman, G. and Ignatov, A.: Derivation of green vegetation fraction from NOAA/AVHRR for use in

1012 numerical weather prediction models, *Int. J. Remote Sens.*, 19: 1533-1543, 1998.

1013 Hanasaki, N., Kanae, S., Oki, T., Masuda, K., Motoya, K., Shirakawa, N., Shen, Y., and Tanaka, K.: An

1014 integrated model for the assessment of global water resources- Part 1: Model description and input

1015 meteorological forcing, *Hydrol. Earth Syst. Sci.*, 12, 1007-1025, doi:10.5194/hess-12-1007-2008, 2008a.

1016 Hanasaki, N., Kanae, S., Oki, T., Masuda, K., Motoya, K., Shirakawa, N., Shen, Y., and Tanaka, K.: An

1017 integrated model for the assessment of global water resources- Part 2: Applications and assessments,

1018 *Hydrol. Earth Syst. Sci.*, 12, 1027-1037, doi:10.5194/hess-12-1027-2008, 2008b.

1019 Jiang, X., Wiedinmyer, C., Chen, F., Yang, Z. L., and Lo, J. C. F.: Predicted impacts of climate and land use

1020 change on surface ozone in the Houston, Texas, area, *J. Geophys. Res.*, 113, D20312,

1021 doi:10.1029/2008JD009820, 2008.

1022 Jin, M. and Shepherd J. M.: Inclusion of urban landscape in a climate model—How can satellite data

1023 help?, *Bull. Am. Meteorol. Soc.*, 86(5), 681–689, DOI:10.1175/BAMS-86-5-681, 2005.

1024 Johnson, T. D. and Belitz K.: A remote sensing approach for estimating 1 the location and rate of urban

1025 irrigation in semi-arid climates, *Journal of Hydrology*, 414-415, 86-98, 2012.

1026 Justice, C. O., Townshend, J. R. G., Vermote, E. F., Masuoka, E., Wolfe, R. E., Saleous, N., Roy, D. P.,  
1027 Morisette, J. T.: An overview of MODIS land data processing and product status. *Remote Sensing of*  
1028 *Environment*, 83(1–2), 3–15, 2002.

1029 Kalnay, E. and Cai, M.: Impact of urbanization and land-use change on climate, *Nature*, 423(29),  
1030 528–531, 2003.

1031 Kusaka, H., Kimura, F.: Thermal effects of urban canyon structure on the nocturnal heat island: Numerical  
1032 experiment using a mesoscale model coupled with an urban canopy model, *J. Appl. Meteorol.* 43: 1899–  
1033 1910, 2004.

1034 Kusaka, H., Kondo, H., Kikegawa, Y., and Kimura, F.: A simple single-layer urban canopy model for  
1035 atmospheric models: Comparison with multi-layer and slab models, *Bound.-Layer Meteorol.*, 101, 329–  
1036 358, 2001.

1037 Landsberg, H. E.: *The urban climate*. New York: Academic Press, 1981.

1038 Latifi, H. and Galos, B.: Remote sensing-supported vegetation parameters for regional climate models: a  
1039 brief review, *iForest* 3: 98-101, doi: 10.3832/ifor0543-003, 2010.

1040 Loridan, T., Grimmond, C. S. B., Grossman-Clarke, S., Chen, F., Tewari, M., Manning, K., Martilli, A.,  
1041 Kusaka, H., Best, M.: Trade-offs and responsiveness of the single-layer urban parameterization in WRF:  
1042 an offline evaluation using the MOSCEM optimization algorithm and field observations, *Q.J.R. Meteorol.*  
1043 *Soc.*, 136: 997–1019. doi: 10.1002/qj.614, 2010.

1044 Lowry, W.: Urban effects on precipitation amount, *Progress in Physical Geography*, 22(4), 477–520, DOI:  
1045 10.1177/030913339802200403, 1998.

1046 Marshall, C. H., Pielke, R. A., Steyaert, L., and Willard, D.: The impact of anthropogenic land-cover  
1047 change on the Florida peninsula sea breezes and warm season sensible weather, *Mon. Wea. Rev.*, 132,  
1048 28–52, doi: <http://dx.doi.org/10.1175/1520-0493>, 2004.

1049 [Martilli, A., Clappier, A., and Rotach, M. W.: An urban surface exchange parameterization for mesoscale](#)  
1050 [models, \*Boundary-Layer Meteorology\* 104: 261–304, 2002.](#)

1051 McPherson, E. G., Simpson, J. R., Xiao, Q., Wu, C.: Los Angeles 1-million tree canopy cover assessment,  
1052 Gen. Tech. Rep. PSW-GTR-207, Albany, CA: U.S. Department of Agriculture, Forest Service, Pacific  
1053 Southwest Research Station, 52 p, 2008.

1054 Miao, S. and Chen F.: Formation of horizontal convective rolls in urban areas, *Atmospheric Research*,  
1055 89(3): 298–304, doi:10.1016/j.atmosres.2008.02.013, 2008.

1056 Miao, S., Chen F., LeMone, M. A., Tewari M., Li, Q., Wang, Y.: An observational and modeling study of  
1057 characteristics of urban heat island and boundary layer structures in Beijing, *J. Appl. Meteor. Climatol.*,  
1058 48, 484–501, doi: <http://dx.doi.org/10.1175/2008JAMC1909.1>, 2009.

1059 Mini, C., Hogue, T. S., ~~and~~ Pincetl, S.: Estimation of Residential Outdoor Water Use in Los Angeles,  
1060 California, Landscape [Urban Plan, 127, 124–135, doi:10.1016/j.landurbplan.2014.04.007, 2014.](#)

Deleted: ., 2014:

Deleted: and Urban Planning (in press)

1061 Moering, D. C.: A comparative study of evapotranspiration rates between irrigated and non-irrigated  
1062 parks in Los Angeles, M.S. thesis, Dep. of Civil and Env. Eng., Univ. of California Los Angeles, Los Angeles,  
1063 California, 2011.

1064 National Oceanographic and Atmospheric Administration-Coastal Services Center (NOAA-CSC): Southern  
1065 California 2000-Era Land Cover/Land Use, LANDSAT-TM, 10m, NOAA-CSC, Charleston, SC, 2003.

1068 National Weather Service (NWS): Jet Stream - The Marine Layer, NOAA National Weather Service,  
1069 <http://www.srh.noaa.gov/jetstream/ocean/marine.htm> (last access: 24 February 2013), 2011.  
1070 Niyogi, D., Holt, T., Zhong, S., Pyle, P. C., and Basara, J.: Urban and land surface effects on the 30 July  
1071 2003 mesoscale convective system event observed in the Southern Great Plains, *J. Geophys. Res.*, 111,  
1072 D19107, doi:10.1029/2005JD006746, 2006.

1073 Pielke, R. A. Sr., Marland, G., Betts, R. A., Chase, T. N., Eastman, J. L., Niles, J. O., Niyogi, D., and Running,  
1074 S.: The influence of land-use change and landscape dynamics on the climate system: Relevance to  
1075 climate change policy beyond the radiative effect of greenhouse gases, *Phil. Trans. R. Soc. London A*,  
1076 360(Special Theme Issue), 1705–1719, 2002.

1077 Pokhrel, Y., Hanasaki, N., Koirala, S., Cho, J., Kim, H., Yeh, P. J.-F., Kanae, S., and Oki, T.: Incorporating  
1078 anthropogenic water regulation modules into a land surface model, *Journal of Hydrometeorology*, 13  
1079 (1), 255-269, doi: 10.1175/JHM-D-11-013.1, 2012.

1080 Sailor, D. J., Lu, L.: A top-down methodology for developing diurnal and seasonal anthropogenic heating  
1081 profiles for urban areas, *Atmospheric Environment* 38: 2737–2748,  
1082 doi:10.1016/j.atmosenv.2004.01.034, 2004.

1083 Schaaf, C. B., Gao, F., Strahler, A. H., Lucht, W., Li, X. W., Tsang, T., Strugnell, N. C., Zhang, X. Y., Jin, Y. F.,  
1084 Muller, J. P., Lewis, P., Barnsley, M., Hobson, P., Disney, M., Roberts, G., Dunderdale, M., Doll, C.,  
1085 d'Entremont, R. P., Hu, B. X., Liang, S. L., Privette, J. L., Roy, D.: First operational BRDF, albedo nadir  
1086 reflectance products from MODIS, *Remote Sensing of Environment*, 83(2-Jan), 135-148, 2002.

1087 Shuai, Y., Masek, J. G., Gao, F., and Schaaf, C. B.: An algorithm for the retrieval of 30-m snow-free albedo  
1088 from Landsat surface reflectance and MODIS BRDF, *Remote Sensing of Environment*, 115, 2204-2216,  
1089 doi:10.1016/j.rse.2011.04.019, 2011.

Deleted: ,

1091 Shuai, Y., Schaaf, C. B., Strahler, A. H., Liu, J., and Jiao, Z.: Quality assessment of BRDF/albedo retrievals  
1092 in MODIS operational system, *Geophysical Research Letters*, 35, L05407, 5PP,  
1093 doi:10.1029/2007GL032568, 2008.

1094 Sobrino, J. A. and Raissouni, N.: Toward remote sensing methods for land cover dynamic monitoring:  
1095 Application to Morocco, *International Journal of Remote Sensing*, 21, pp. 353–366  
1096 DOI:10.1080/014311600210876, 2000.

1097 Sobrino, J. A., Raissouni, N., and Li, Z. L.: A comparative study of land surface emissivity retrieval from  
1098 NOAA data. *Remote Sensing of Environment*, 75, pp. 256–266, 2001.

1099 Song, M. and Civco, D. L.: A knowledge-based approach for reducing cloud and shadow, *Proceedings of*  
1100 *the American Society of Photogrammetry and Remote Sensing annual convention*, Washington, DC:  
1101 *American Society of Photogrammetry and Remote Sensing*, 7 p, 2002.

1102 State of California Department of Water Resources (SCDWR): California irrigation management  
1103 information system, Sacramento, CA: State of California Department of Water Resources, Available at:  
1104 <http://www.water.ca.gov/>, 2009.

1105 Stathopoulou, M. and Cartalis, C.: Daytime urban heat islands from Landsat ETM+ and Corine land cover  
1106 data: An application to major cities in Greece, *Solar Energy*, 81 (3), pp. 358-368,  
1107 doi:10.1016/j.solener.2006.06.014, 2007.

1108 Stathopoulou, M., Cartalis, C., and Petrakis, M.: Integrating Corine Land Cover data and Landsat TM for  
1109 surface emissivity definition: application to the urban area of Athens, Greece, *International Journal of*  
1110 *Remote Sensing*, 28:15, 3291-3304, DOI:10.1080/01431160600993421, 2007.

1111 Stenberg, P., Rautiainen, M., Manninen, T., Voipio, P., and Smolander, H.: Reduced simple ratio better  
1112 than NDVI for estimating LAI in Finnish pine and spruce stands, *Silva Fennica* 38(1): 3–14, 2004.

1113 Taha, H., Ching, J. K. S.: UCP/MM5 Modeling in conjunction with NUDAPT: model requirements, updates,  
1114 and applications, Seventh Symposium on the Urban Environment, San Diego, CA, 10–13 September,  
1115 American Meteorological Society: Boston, MA, Paper 6.4, 2007.

1116 Taha, H., Douglas, S., and Haney, J.: Mesoscale meteorological and air quality impacts of increased urban  
1117 albedo and vegetation, *Energy and Buildings*, 25, 169–177, DOI: 10.1016/S0378-7788(96)01006-7, 1997.

1118 Taha, H.: Meso-urban meteorological and photochemical modeling of heat island mitigation,  
1119 *Atmospheric Environment*, 42: 8795–8809, DOI:10.1016/j.atmosenv.2008.06.036, 2008.

1120 Taha, H.: Modifying a mesoscale meteorological model to better incorporate urban heat storage: a bulk-  
1121 parameterization approach, *J. Appl. Meteorol.*, 38, 466–473, doi:10.1175/1520-  
1122 0450(1999)038<0466:MAMMMT>2.0.CO;2, 1999.

1123 Tan, M. and Li, X.: Integrated assessment of the cool island intensity of green spaces in the mega city of  
1124 Beijing, *International Journal of Remote Sensing*, 34:8, 3028-3043, DOI:  
1125 10.1080/01431161.2012.757377, 2013.

1126 Tewari, M., Kusaka, H., Chen, F., Coirier, W. J., Kim, S., Wyszogrodzki, A., Warner, T. T.: Impact of  
1127 coupling a microscale computational fluid dynamics model with a mesoscale model on urban scale  
1128 contaminant transport and dispersion, *Atmospheric Research* 96: 656–664,  
1129 doi:10.1016/j.atmosres.2010.01.006, 2010.

1130 US Census: US Census Bureau Releases Data on Population Distribution and Change in the US Based on  
1131 Analysis of 2010 Census Results, US Census Bureau, 24 March 2011.

1132 Vahmani, P. and Hogue, T. S.: Modelling and analysis of the impact of urban irrigation on land surface  
1133 fluxes in the Los Angeles metropolitan area, *Climate and Land Surface Changes in Hydrology Proceedings*  
1134 of H01, IAHS-IAPSO-IASPEI Assembly, Gothenburg, Sweden, July 2013, IAHS Publ. 359, 2013.

Deleted: Meteor

Deleted: http://dx.doi.org/

Deleted: U.S.

Deleted: U.S.

Deleted: U.S.

Deleted: U.S.

Deleted: 24,

1142 Vahmani, P. and Hogue, T. S.: Incorporating an Urban Irrigation Module into the Noah Land Surface  
1143 Model Coupled with an Urban Canopy Model, [J. Hydrometeorol.](#), doi:10.1175/JHMD-13-0121.1, in press,  
1144 [2014](#).

1145 Van Wevenberg, K., De Ridder, K., Van Rompaey, A.: Modeling the contribution of the Brussels heat  
1146 island to a long temperature time series, *Journal of Applied Meteorology and Climatology*, 47, 976e990,  
1147 DOI: 10.1175/2007JAMC1482.1, 2008.

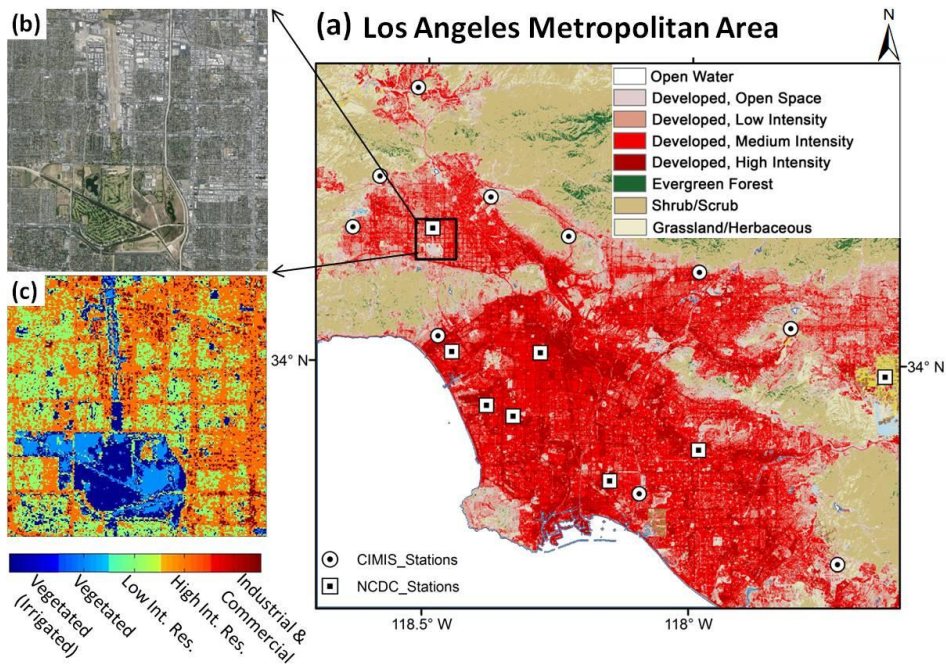
1148 Wang, X. M., Chen, F., Wu, Z. Y., Zhang, M. G., Tewari, M., Guenther, A., and Wiedinmyer, C.: Impacts of  
1149 weather conditions modified by urban expansion on surface ozone: comparison between the Pearl River  
1150 Delta and Yangtze River Delta regions, *Adv. Atmos. Sci*, 26(5), 962-972, doi: 10.1007/s00376-009-8001-2,  
1151 2009.

1152 Wang, Z. H., Bou-Zeid, E., Au, S. K., and Smith, J. A.: Analyzing the sensitivity of WRF's single-layer urban  
1153 canopy model to parameter uncertainty using advanced Monte Carlo simulation, *J. Appl. Meteor.*  
1154 *Climatol.*, 50, 1795–1814, doi: <http://dx.doi.org/10.1175/2011JAMC2685.1>, 2011.

1155 Wei-guang, M., Yan-xia, Z., Jiang-nan, L., Wen-shi, L., Guang-feng, D., and Hao-ru, L.: Application of  
1156 WRF/UCM in the simulation of a heat wave event and urban heat island around Guangzhou, *Journal of*  
1157 *Tropical Meteorology*, 03, 257-267, doi: 10.3969/j.issn.1006-8775.2011.03.007, 2011.

1158

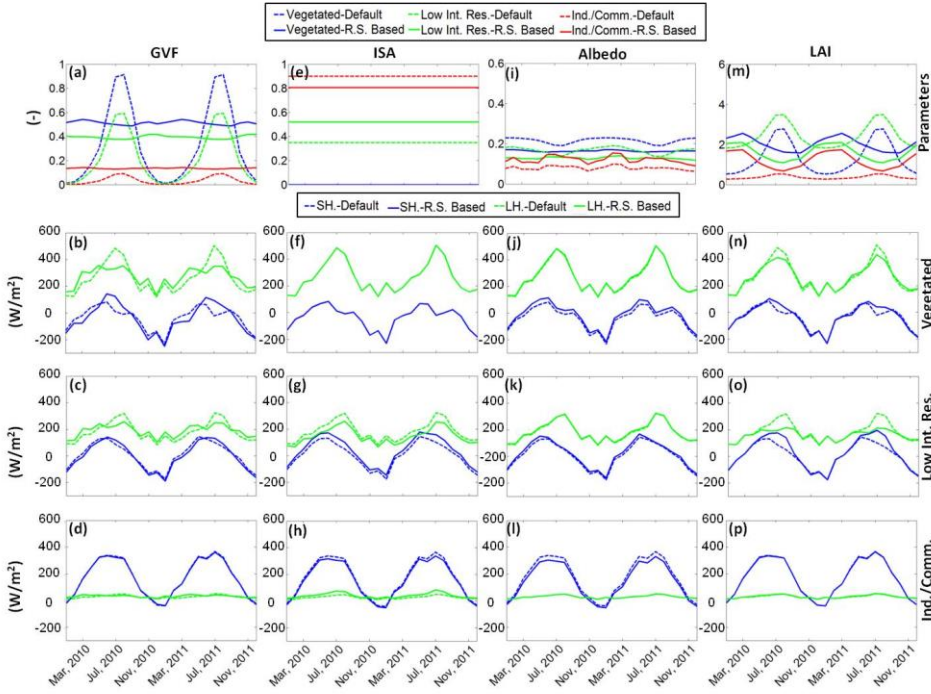
**Deleted:** Journal of Hydrometeorology, 2014 (in press).



1162 **Figure 1.** (a) NOAA C-CAP Land cover map of the Los Angeles metropolitan area including study domain, 10  
1163 CIMIS stations (white circles), and 8 NCDC stations (white squares), (b) Google image of the study domain, and  
1164 (c) The Noah/UCM urban land cover classification of the study domain.

Deleted: 1





1175

1176

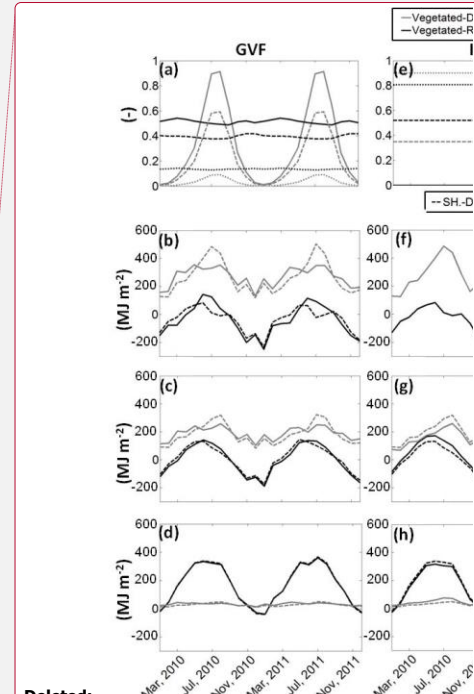
1177

1178

1179

Figure 2. Monthly time series of default Noah/UCM compared with remote sensing based GVF, ISA, albedo, and LAI (row 1) and modeled cumulative monthly sensible and latent heat fluxes ( $\text{MJ m}^{-2}$ ) over fully vegetated, low intensity residential, and industrial/commercial areas using the default and newly estimated parameters: (b-d) GVF, (f-h) ISA, (j-l) albedo, and (n-p) LAI.

1180



Deleted:

Deleted: 2

Deleted: a,e, i, and m

Deleted: ,

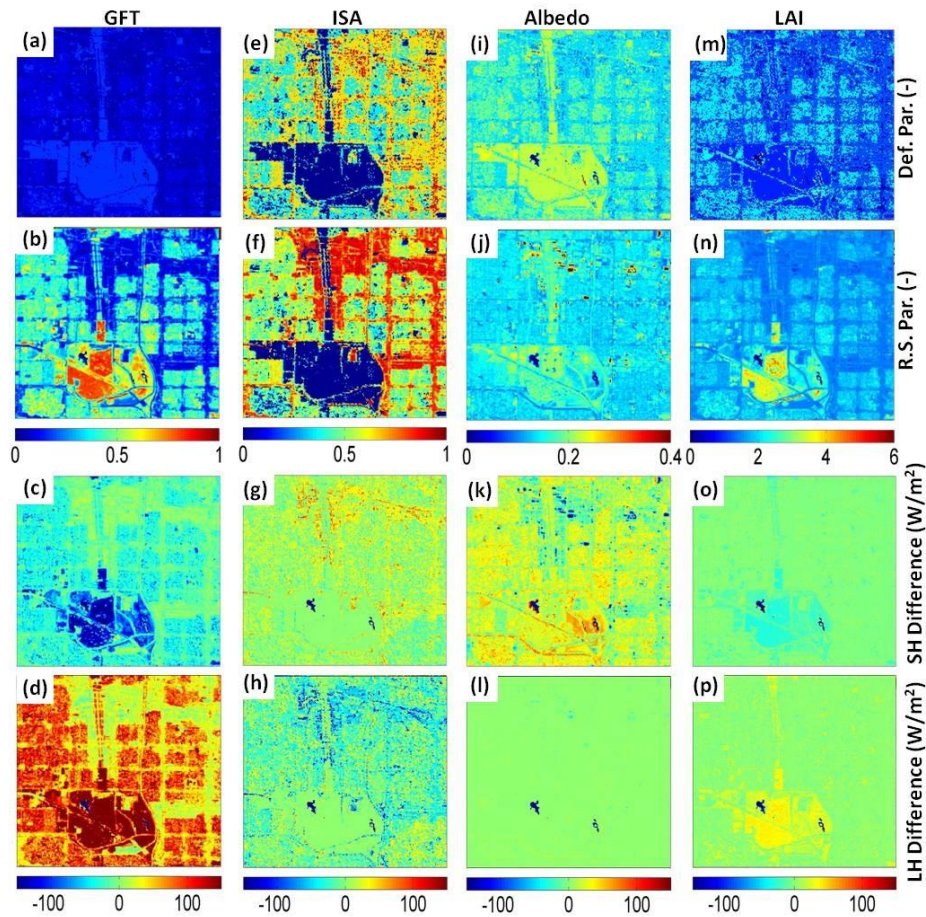
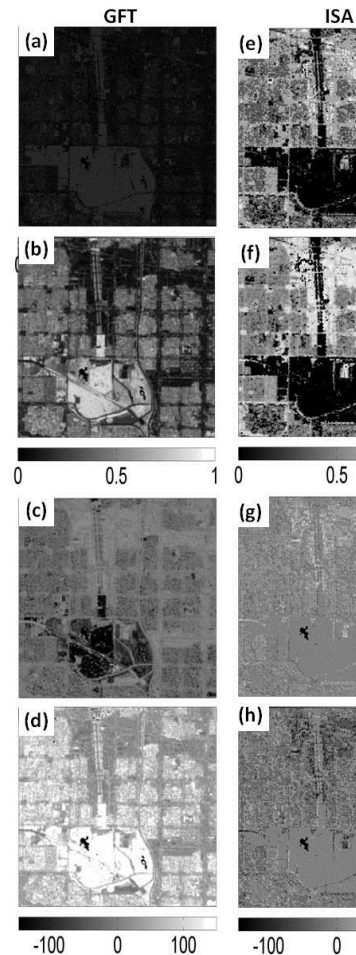


Figure 3. Spatial distributions of GVF, ISA, albedo, and LAI based on Noah/UCM lookup tables (row 1) compared with remotely sensed values (row 2) and simulated difference maps of sensible (row 3) and latent (row 4) heat fluxes using default and remotely sensed urban surface parameters: (c and d) GVF, (g and h) ISA, (k and l) albedo, and (o and p) LAI. Valid at 1100 LST on 14 April 2011.



Deleted:

Deleted: 3

Deleted: remote sensing based

Deleted: (a, e, i, and m) compared with those

Deleted: b, f, j, and n

Deleted: turbulent

1185

1186

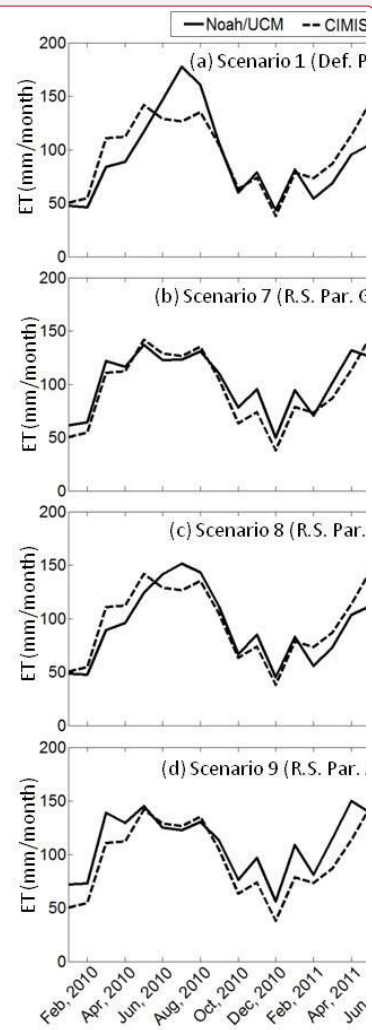
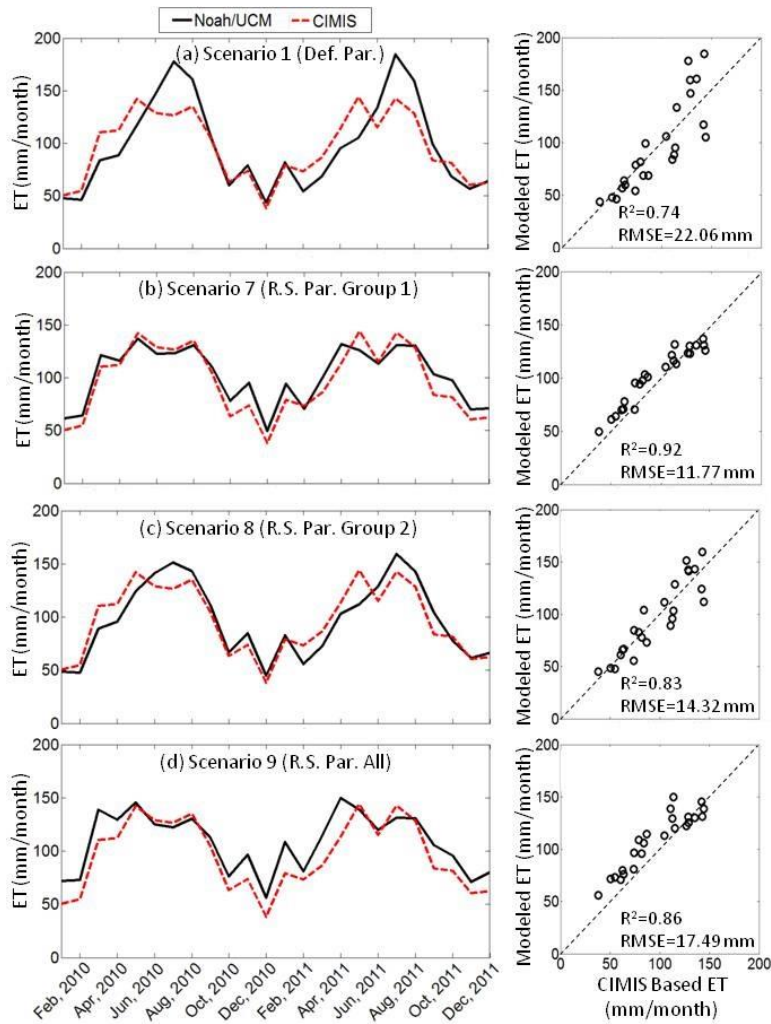
1187

1188

1189

1190

1191



Deleted:  
Deleted: 4

1198

1199

1200

1201

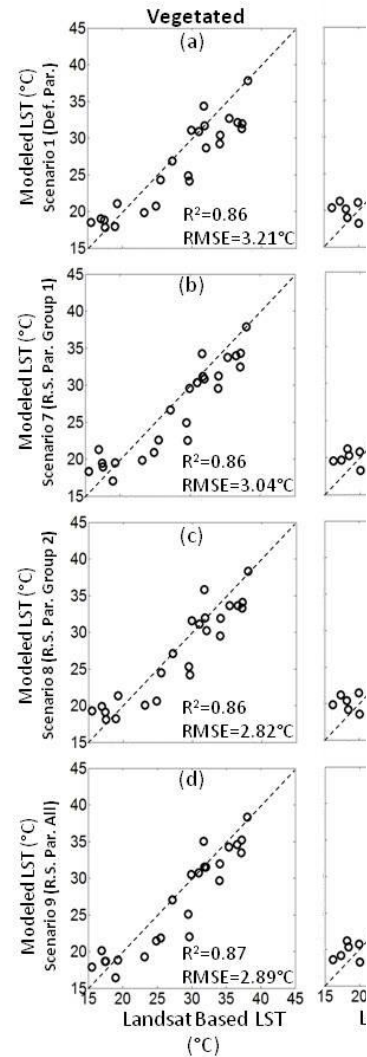
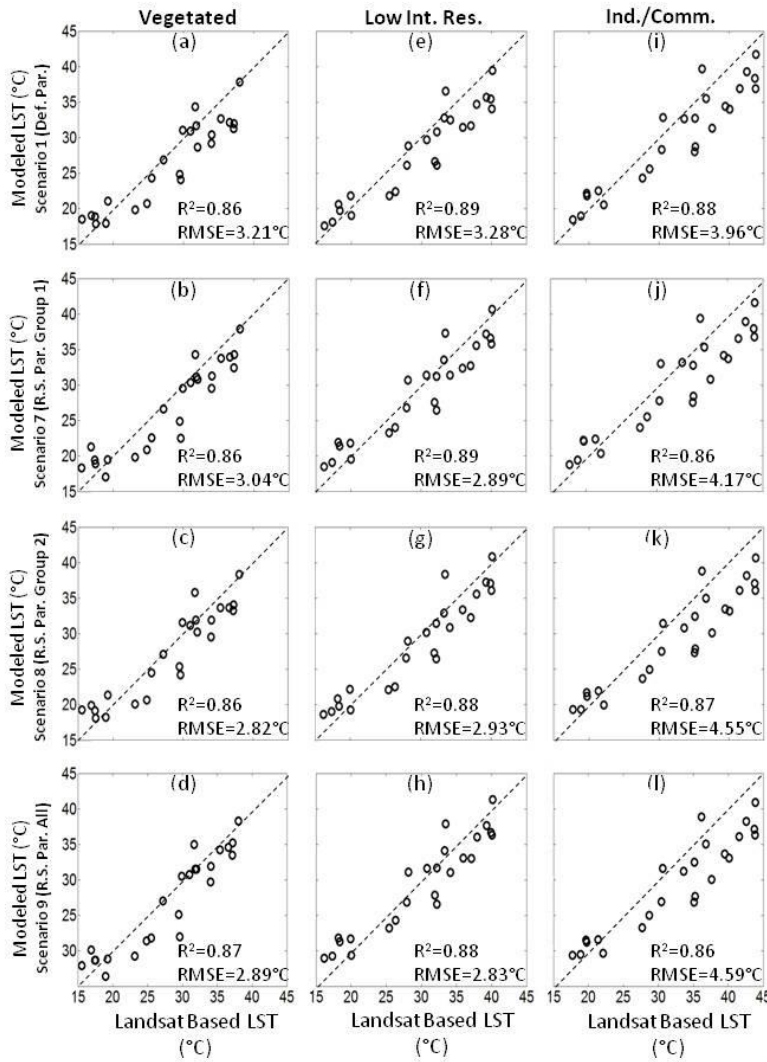
1202

1203

1204

Figure 4. Noah/UCM simulated cumulative monthly ET, averaged over fully vegetated pixels using different urban surface parameterizations: scenarios (a) 1, (b) 7, (c) 8, and (d) 9 in the table 1 and their comparisons with CIMIS-based ET measurements spanning 2010 and 2011. Scatter plots of these comparisons are also included (right).

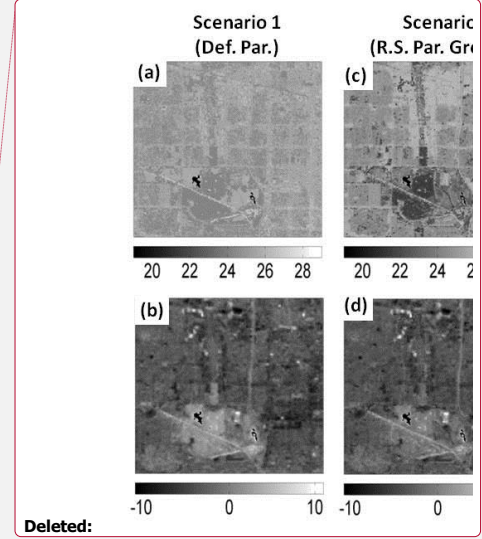
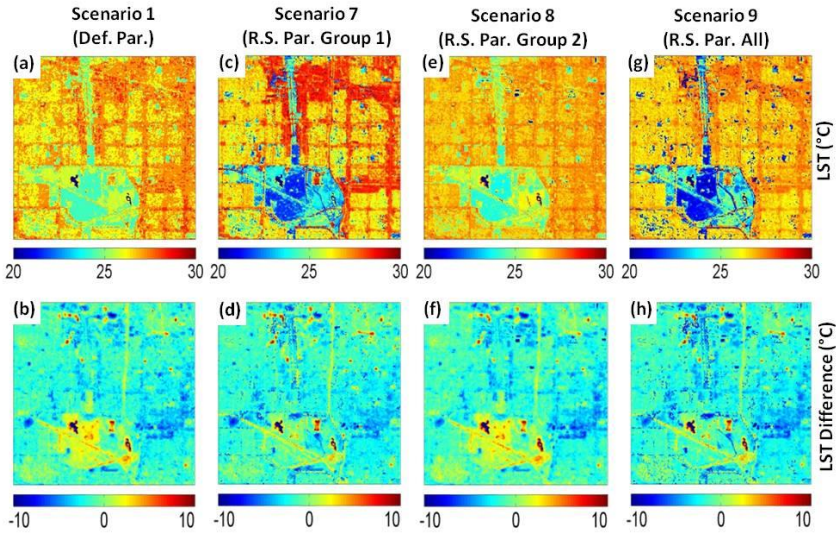




Deleted:  
 Deleted:  
 Deleted: 5

Figure 5. Scatter plots of observed (Landsat-based) versus simulated LSTs averaged over different land cover types using different urban surface parameterizations, including scenarios 1 (first row), 7 (second row), 8 (third row), and 9 (forth row) in Table 1.

1207  
 1208  
 1209  
 1210  
 1211



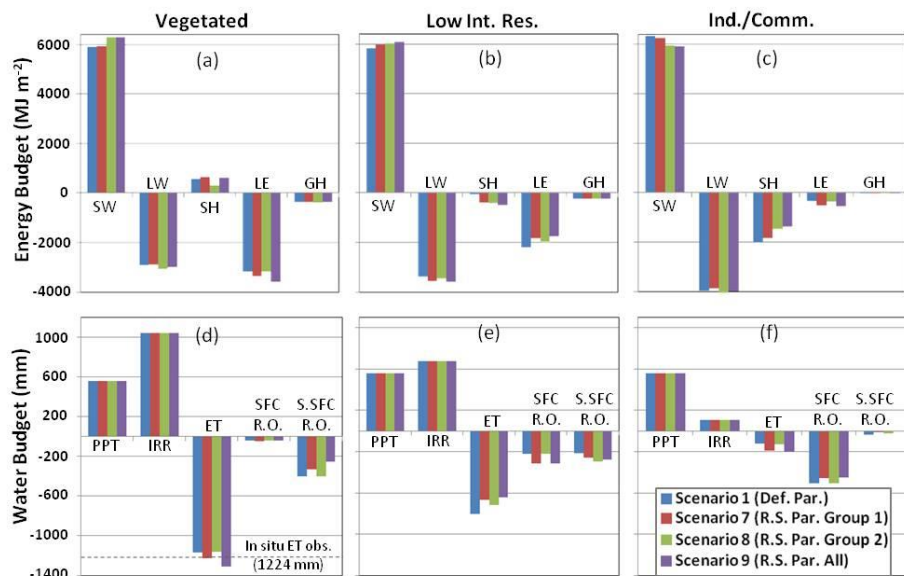
Deleted:

1215  
1216  
1217  
1218  
1219

Figure 6. Noah/UCM simulated LST maps using different urban surface parameterizations: scenarios 1, 7, 8, and 9 from Table 1 (top row) as well as differences between simulated and observed land surface temperature at 1100 LST on 14 April 2011 (bottom row).

Deleted:  
Deleted: 6

1223



1224

Figure 7. Differences in simulated energy (top) and water (bottom) budgets for WY 2011, using different urban surface parameterization and averaged over different land cover types. Energy budget terms include: shortwave radiation (SW), longwave radiation (LW), and sensible (SH), latent (LH), and ground (GH) heat fluxes. Water budget terms include: precipitation (PPT), irrigation water (IRR), evapotranspiration (ET), surface runoff (SFC R.O.), and sub-surface runoff (S.SFC R.O.).

1230

1231

1232

1233

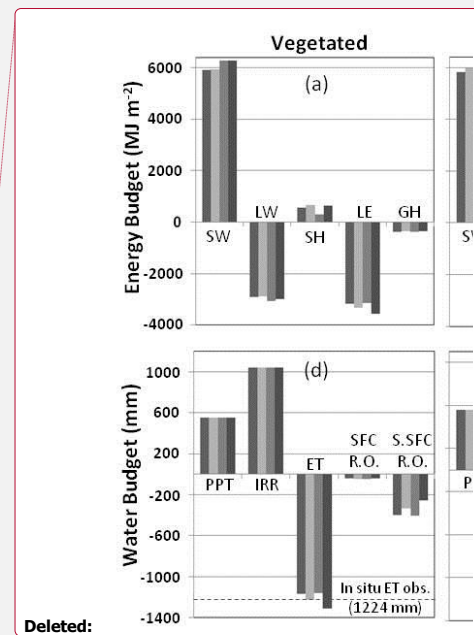
1234

1235

1236

1237

1238



Deleted:

1240

1241

1242

**Table 1. Model scenarios (1-9) and the incorporated remotely sensed parameter sets.**

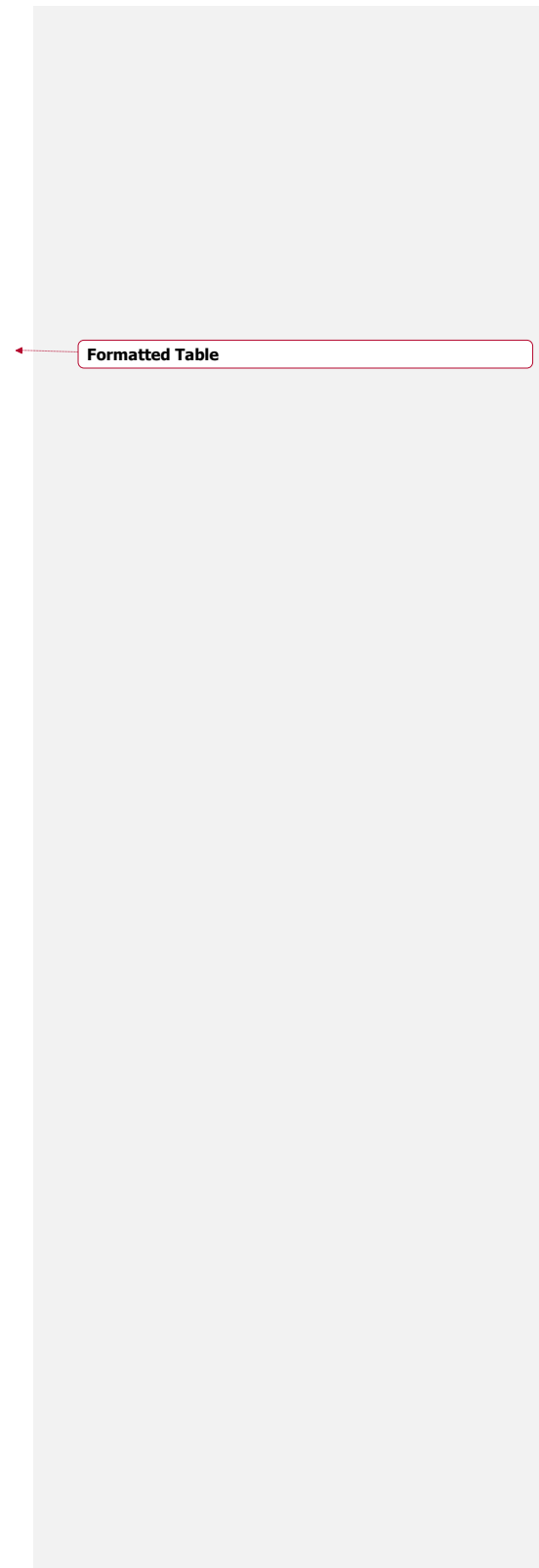
	GVF	ISA	Albedo	LAI	Emissivity
Scenario 1 (Def. Par.)	-	-	-	-	-
Scenario 2 (R.S. GVF)	X	-	-	-	-
Scenario 3 (R.S. ISA)	-	X	-	-	-
Scenario 4 (R.S. Albedo)	-	-	X	-	-
Scenario 5 (R.S. LAI)	-	-	-	X	-
Scenario 6 (R.S. Emissivity)	-	-	-	-	X
Scenario 7 (R.S. Par. Group 1)	X	X	-	-	-
Scenario 8 (R.S. Par. Group 2)	-	-	X	X	X
Scenario 9 (R.S. Par. All)	X	X	X	X	X

1243

1244

1245

1246



Formatted Table